EARTHQUAKE INTERACTION ALONG THE
SULTANDAGI-AKSEHIR FAULT
BASED ON InSAR AND COULOMB STRESS MODELING

_____

A Thesis presented to the Faculty of the Graduate School
University of Missouri-Columbia

_____

In Partial Fulfillment
Of the Requirements for the Degree

Master of Science

_____

By

DEEPAK MANJUNATH

Dr. Francisco Gomez, Thesis Supervisor

MARCH 2008

The undersigned, appointed by the Dean of the Graduate School,
Have examined the thesis entitled

EARTHQUAKE INTERACTION ALONG THE SULTANDAGI-AKSEHIR FAULT
BASED ON INSAR AND COULOMB STRESS MODELING

Presented by Deepak Manjunath

A candidate for the degree of Master of Science in Geology

And hereby certify that in their opinion it is worthy of acceptance.

_____
Professor Francisco Gomez

_____
Professor Eric Sandvol

_____
Professor Justin J. Legarsky

OM SAI RAM

ACKNOWLEDGEMENTS

I owe thanks to a lot of people for enabling me obtain this degree. First and foremost, I thank my family for being supportive and for being patient with me all the way. A lot of thanks also go to my fiancé, Indrani Tulasi, who always encouraged me to pursue my interests.

I would like to express deep gratitude to Dr. Eric Sandvol and Kristin Sandvol for giving me the opportunity that opened up avenues for pursuing this degree. Paco Gomez, has been a great mentor and friend. I thank him for his time, patience, guidance, for encouraging me to think creatively and for all the conversations over coffee.

The Geotechnical Engineering program, of which I have been a part while pursuing this degree, has been instrumental in instilling virtues of commitment, dedication and hard work in me.

I consider myself fortunate to have been in the company of excellent human beings who have made my stay at the University of Missouri, Columbia memorable.

TABLE OF CONTENTS

LIST OF FIGURES

LIST OF TABLES

ABSTRACT

The evolution of geologic structures along active faults is influenced by crustal deformation associated with several repetitions of the earthquake cycle, in addition to surficial processes accompanying geologic time. Within this theme, this study focuses on the Sultandagi-Aksehir Fault (SAF), which bounds the Aksehir-Afyon graben and the Sultan Dag range, in southwestern Turkey. The SAF has been associated with several large earthquakes over the past several centuries. During the past decade, a sequence of moderate-size earthquakes occurred along the SAF, including a M_w 6.0 earthquake (December 15th, 2000) and a M_w 6.5 earthquake (February 3rd, 2002). These earthquakes provide an opportunity to study earthquake interactions along adjacent fault patches. This study investigates the 2000-2002 earthquakes with respect to coulomb stress migration and the implications of the same in terms of stress changes on adjacent fault segments. To address these questions, maps of co-seismic surface displacements were produced using Synthetic Aperture Radar Interferometry (InSAR). The resulting displacement maps provided a basis for estimating faulting parameters associated with each earthquake (fault orientation and slip) using elastic dislocation models. These fault models were subsequently used to estimate static coulomb stress changes resulting from the earthquakes. The findings suggest that although the two events of December 15, 2000, were not directly related to one another in terms of stress triggering, both events can be related to the 2002 earthquake in terms of stress triggering and extent of rupture.

1. INTRODUCTION

1.1 Overview

The evolution of geologic structures along active faults is influenced by crustal deformation associated with several repetitions of the earthquake cycle in addition to surficial processes accompanying geologic time (King et al., 1988). The Aksehir-Afyon graben, located in south-western Turkey (Figure 1.1 and Figure 1.2) and bounded by Sultandagi-Aksehir Fault (SAF), has been associated with numerous large earthquakes over the past several centuries. The earliest available documentation of events occurring in the region dates back to 94 AD, while the formation of the graben itself has been dated to have begun in the Pliocene (Ozer, 2006).
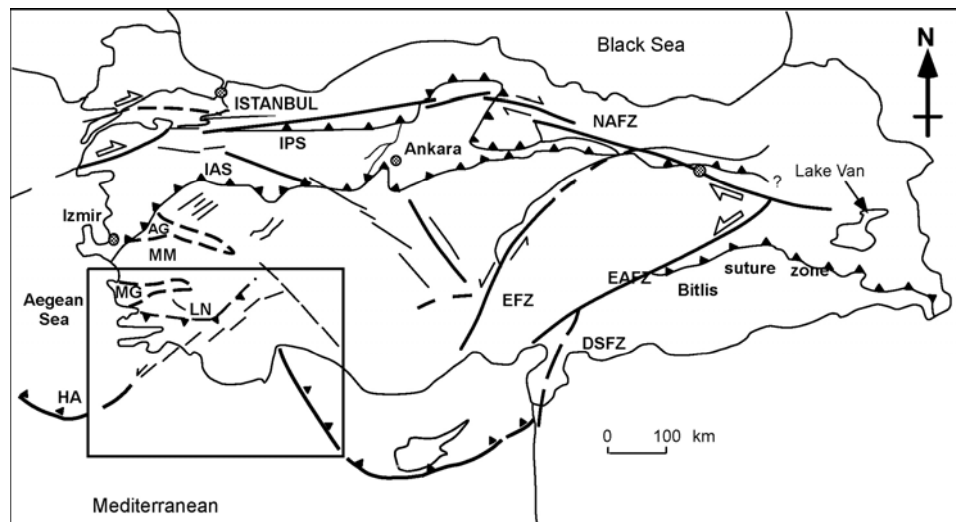
Figure 1.1 Generalized tectonic map of Turkey. NAFZ=North Anatolian fault zone, EAFZ=East Anatolian fault zone, DSFZ= Dead Sea fault zone, IAS=Izmir-Ankara suture zone, EFZ=Ecemis fault zone, HA=Hellenic Arc.

Recent seismic activity in the vicinity of the SAF has been marked by two moderate size events viz., the M_w 6.0 Sultandagi Aksehir earthquake dated 15th December 2000 and the M_w 6.5 Cay-Eber earthquake dated February 3rd, 2002 (Ozer, 2006). The M_w 6.5 February 3rd, 2002 earthquake occurred at 09:11:28 GMT on the SAF and was followed by three aftershocks greater than M_w 5. The largest aftershock (M_w 6.0) occurred about two hours after the main event. A total of 26 km of surface is reported to have ruptured during the February 2002 event. In addition, 21 cm of vertical displacement, 15 cm of extension and 10 cm of left lateral horizontal displacement were recorded at the ruptured segments (Emre et al., 2003).
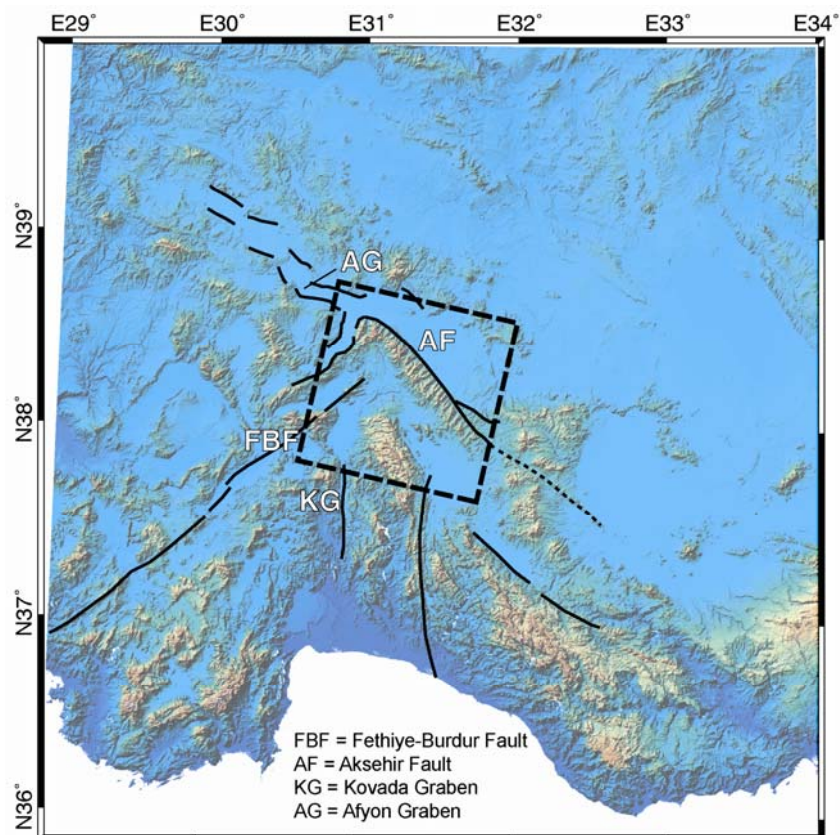
Figure 1.2 Topographic map of south-western Turkey. Bold lines demarcate faults in the region. The study area has been delineated by the dashed box.

The spatial and temporal proximity of the occurrence of the 2000 and 2002 events must be considered in the context of the effect of redistribution of stresses released by these events on regional tectonism and incremental uplift of the Sultandag mountain range. Irrespective of prevalent stress environments and tectonic settings, correlation between main shock and after shock locations and, in some cases, future main shock locations, has been explained by means of static Coulomb stress changes occurring on fault segments in the vicinity of the main shock (Lin and Stein, 2004).

Due to the excellent spatial coverage, tens of meters of spatial resolution and millimetric sensitivity to surface deformation that is achievable from Synthetic Aperture Radar Interferometry (InSAR), the technique finds wide use as a space based geodetic tool. Owing to the advantages associated with InSAR, the technique was used in this study to derive surface displacement maps corresponding to the two events. The surface displacements derived from InSAR were used to constrain a fault model which was then used to infer static coulomb stress changes resulting from the two events

1.2 Tectonic Setting

The study area is part of the Isparta Angle (IA), which occupies a unique location in the over-riding plate above the Hellenic and Cyprus subduction zones. The Sultandagi-Aksehir fault (SAF) outlines the Aksehir-Afyon Graben (AAG) and forms the north-eastern boundary of the IA region. The SAF is a normal fault and is characterized by a dip slip rate of 0.3 mm/y (Kocyigit and Ozacar, 2003). The

Fethiye Burdur fault zone (FBFZ) that lies approximately perpendicular to the SAF forms the western boundary of the IA region.

The IA is defined by the intersection of the Hellenic and Cyprus arcs formed due to the subduction of the Africa plate beneath the Anatolian plate (Barka et al., 1997). The right lateral North Anatolian Fault Zone (NAFZ) and the left lateral East Anatolian Fault Zone (EAFZ) are the two major fault zones that demarcate the Anatolian plate.

The Anatolian plate is marked by a westward escape (Figure 1.3) attributed mainly to the convergence between the Asian and Arabian plates as well as subduction rollback along the Hellenic arc (e.g., McClusky et al., 2000, Reilinger et al., 2006).
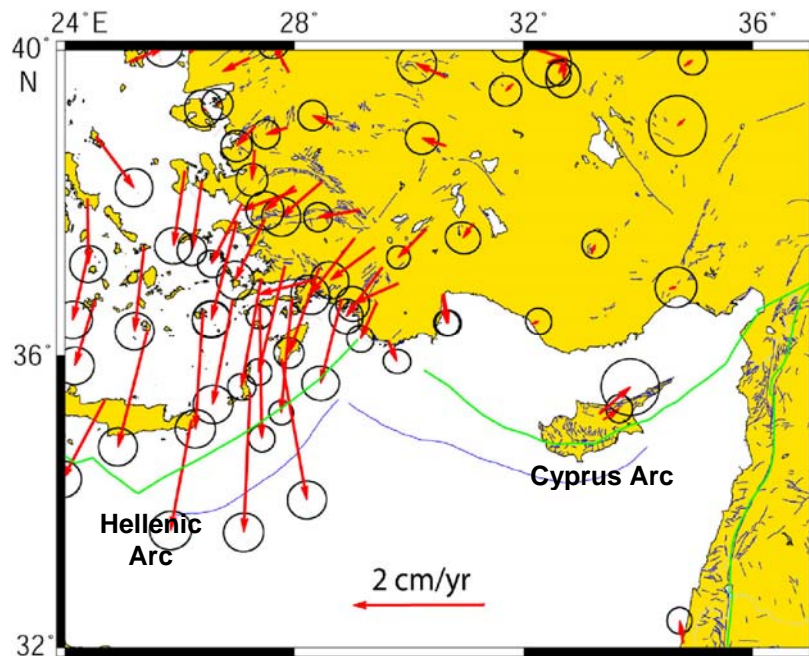
Figure 1.3 GPS vectors for south-western Turkey (McClusky et al., 2000).

Subduction along the Hellenic arc is known to be steep whereas subduction along the Cyprus arc is known to be shallower in comparison. Arc

normal extension is representative of the nature of deformation behind the Hellenic arc, whereas deformation behind the Cyprus arc is representative of arc parallel extension, which of suggestive of the compressional environment characterizing the Cyprus arc. Focal mechanisms in the vicinity of the IA (Figure 1.4) reveal a transition from thrust faulting events near the Hellenic arc to normal faulting events near the IA whereas focal mechanisms near the Cyprus arc are indicative of thrust faulting events.
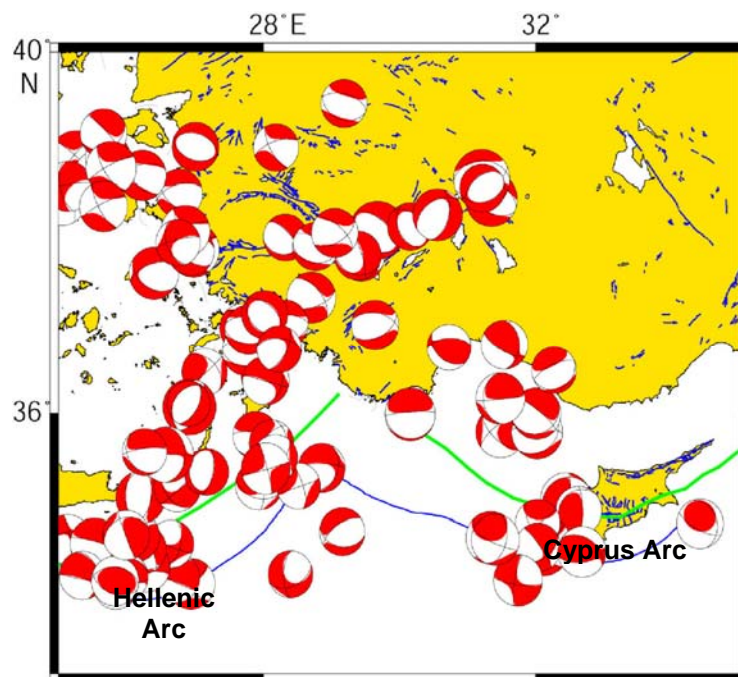
Figure 1.4 Focal mechanisms for south-western Turkey (Ekstrom et al., 2005).

GPS velocity vectors for regions within the IA are indicative of counter-clockwise motion relative to the Eurasian plate, independent of the rest of the Anatolian plate, suggestive of such plate motion being influenced by subduction rollback along the Hellenic arc (Barka et al., 1997, McClusky et al., 2000).

1.3 Objectives

This study was formulated to achieve the following objectives:

1. To use Synthetic aperture radar (InSAR) to measure co-seismic crustal displacement estimates corresponding to the 2000 and 2002 earthquakes.

2. The use of InSAR derived co-seismic crustal displacement estimates to constrain a fault model of the SAF.

3. Static coulomb stress analysis of the stress redistribution resulting from the 2000-2002 sequence of events to address the following:

    a) Whether the 2000-2002 earthquakes can be explained in terms of coulomb stress migration, and

    b) Implications of the 2000-2002 earthquakes in terms of stress changes imparted on fault segments adjacent to the ones that ruptured during the main events.

2. METHODS

2.1 Introduction

As mentioned in Chapter 1, crustal deformation resulting from the two seismic events considered for this study was inferred using InSAR. These estimates of deformation were used to constrain fault models which were then used to infer resulting static Coulomb stress changes on faults located in the study area. This chapter introduces the concept of Synthetic Aperture Radar Interferometry (InSAR) as applied to Synthetic Aperture Radar data.

2.2 Overview of Synthetic Aperture Radar

The synthetic aperture radar concept, initially referred to as Doppler beam sharpening, is attributed to Carl Wiley, who in 1951 made the observation that it was possible to use the difference in Doppler frequency shift induced by two distinct targets within a radar beam in order to improve the resolving power of the moving radar in the direction of its flight (Curlander and McDonough, 1991). The synthetic aperture radar, as it is known today, is a pulsed-radar that uses the forward motion of the platform carrying it in order to simulate an antenna with a larger aperture.

The aperture can be defined as "the physical area of the antenna projected onto a plane perpendicular to the direction of the antenna beam" (Maini and Agrawal, 2007). The antenna beam is a channel of electromagnetic energy radiated by the antenna (Skolnik, 1962). The resolution of traditional radar systems is a function of the angular resolution of the radar beam and its altitude

of operation. The angular resolution is inversely proportional to the length of the antenna aperture. Hence, high operating altitudes will need to be compensated by long antenna apertures to preserve the resolution of such systems. Hence achieving high resolutions with traditional radar systems entails impractically long antennas (several kilometers) to be mounted on imaging platforms. Using SAR, the unfeasibility of mounting large real aperture radars on moving platforms like aircrafts or satellites for high resolution data acquisition is overcome by synthesizing large antenna lengths by using the forward motion of the antenna during imaging. Thus an object on the ground is imaged from many different locations on the satellite's flight track.

The redundancy in information, obtained by recording the backscatter from the object when imaged from different perspectives, is then used to generate high resolution digital imagery. The component of electromagnetic energy reflected by objects on the ground towards the antenna is called backscatter.

Electromagnetic radiations with frequencies ranging from 1-GHz to 300-GHz define the microwave region of the electromagnetic spectrum. Satellite-borne SAR systems operate in the 1-GHz to 10-GHz window of microwave frequencies and are classified according to the specific frequency bands they adopt for imaging. All SAR's are active microwave remote sensing systems meaning that the radar illuminates the target to be imaged with electromagnetic radiation. The long wavelengths characteristic of microwave frequencies enable

cloud penetration. Moreover, the ability to illuminate the object being imaged enables night-time data acquisition.
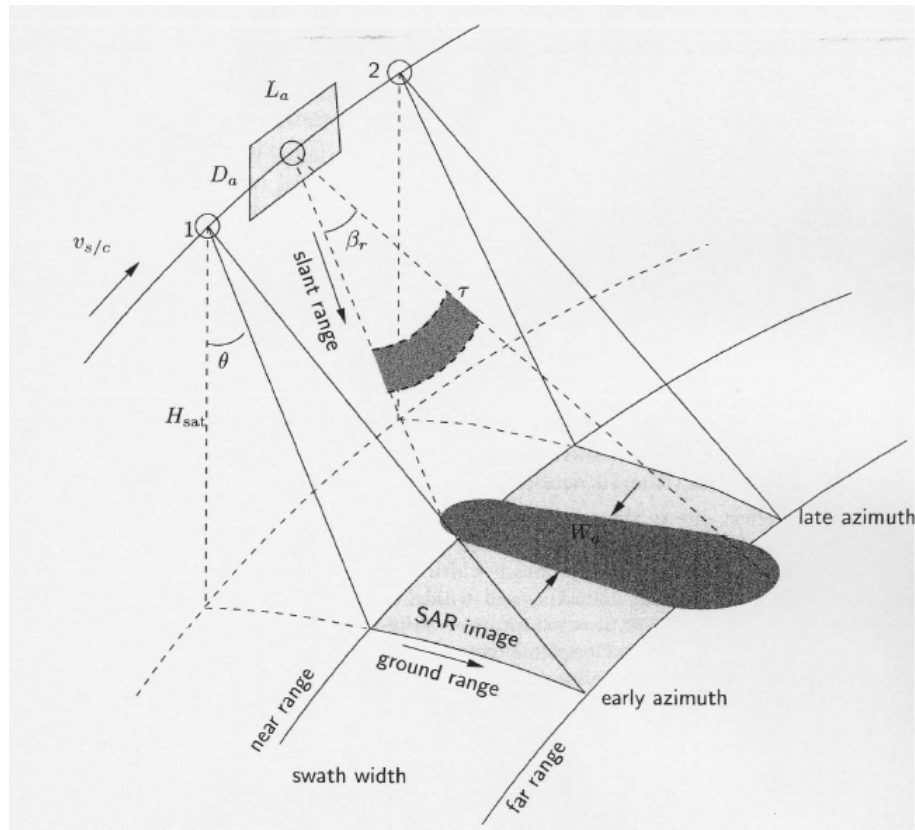
Figure 2.1 SAR imaging geometry (Hanssen, 2001).

2.2.1 Overview of SAR Systems

Synthetic Aperture Radars (SAR's) used to acquire data for interferometry are usually mounted on either satellite or airborne platforms. Examples of airborne SAR systems include AIRSAR, DCS, IFSARE, P-3/SAR,C/X-SAR, STAR-1 and STAR-2 while examples of satellite borne SAR systems include Seasat, SIR-A/B/C, X-SAR, ERS-1/2, Envisat, JERS-1, RADARSAT-1/2, and TerraSAR-X.

Specifications of some satellite borne SAR systems have been provided in Table 2.1. The repeat cycle defines the time period between successive visits by the satellite to image the same location on the ground. The operating frequency (f_0) defining a mission is directly related to the wavelength of microwave radiation used for imaging while the bandwidth defining a SAR system governs the achievable range resolution. The look angle (θ) in Table 2.1, is the look angle at the center of the swath.

Table 2.1 Satellite-borne SAR system specifications (Hanssen, 2001 and Eineder et al., 2004)

Mission	Launch Year	Repeat Cycle (days)	Satellite Altitude (km)	f_0 (GHz)	Bandwidth (MHz)	Look Angle (degrees)
ERS-1	1991	35	790	5.3	15.55	23
ERS-2	1995	35	790	5.3	15.55	23
JERS-1	1992	44	568	1.275	15	39
Radarsat-1	1995	24	792	5.3	11-30	20-49
ENVISAT	2001	35	800	5.3	14	20-50
ALOS	2002	45	700	1.27	28	8-60
TerraSARX	2007	11	514	10	150	~35

2.2.2 SAR Data Acquisition

During data acquisition, the SAR transmits electromagnetic waves with microwave frequencies ranging from 1 GHz – 10 GHz towards the Earth and records the magnitude and phase of the fraction of the incident energy reflected back towards the satellite. Such systems recording both the amplitude and phase of the reflected energy or echoes are known as coherent imaging systems (Curlander and McDonough, 1991). During data acquisition, the SAR is pointed

towards the Earth in a plane that is orthogonal to the direction of flight of the platform carrying it. The angle made by the radar look vector with respect to the vertical is known as the off-nadir angle or the look angle and gives rise to the side looking geometry of the SAR during data acquisition as shown in Figure 2.1.

The SAR images a particular object on the ground from several different locations during the satellite's orbit. For example, an object on the ground is typically imaged from around 1000 different locations in the orbit of the ERS-1 (ESA, 2007). These various responses are then digitally processed in order to assign the object a distinct amplitude and phase. The distance on the satellite's trajectory defining the time period during which an object on the ground begins and stops being imaged or detected by the SAR is known as the length of the synthesized aperture. As an example, the 10-m long imaging radar mounted on the ERS-1 images objects on the ground for a distance of 4 km during its orbit. In other words, the ERS-1 synthesizes the resolution achievable with a 4-km long antenna using an antenna that is only 10-m long (ESA, 2007).

An image of a location on Earth that is illuminated by electromagnetic radiation from SAR platforms can be constructed by processing the radar echoes recorded by the satellite during image acquisition. The processed SAR image is composed of evenly spaced pixels. Each pixel denotes the information corresponding to a ground resolution cell (Hanssen, 2001). A ground resolution cell, whose dimensions are defined by the ground range resolution and ground azimuth resolution of a SAR system, can be defined as the area on the ground that corresponds to a single pixel as mapped in a SAR image. The

electromagnetic radiation reflected towards the SAR system from all elements located within a ground resolution cell, eg. buildings, roads, etc., contribute to the backscatter that is associated with the pixel representing the ground resolution cell in the SAR image**.**

The data corresponding to each pixel in a SAR image can be represented as a complex number having amplitude and phase. Owing to details pertaining to the process in which raw SAR data are processed into a SAR image and owing to the complex number representation of data for each pixel in the SAR image, the processed SAR image is also referred to as a Single Look Complex (SLC) image. Resolution cells characterized with high amplitudes of backscatter show up as bright pixels on the processed SAR image whereas those with low backscatter are characterized by darker colors.

The amplitude of a pixel is a function of its overall roughness. Rough surfaces reflect more of the incident electromagnetic energy back to the radar resulting in high amplitudes whereas smooth surfaces reflect the incident energy in a direction away from the satellite and result in low amplitudes.

The differential path delay phase of a scattering element in a SAR image resolution cell represents the change in phase between the transmitted and received signals owing to the time taken by the signal to traverse the two-way distance between the satellite and the element on the ground. Eq. 2.1 denotes the mathematical expression for the differential path delay phase (ϕ) of an elemental scatterer within a resolution cell.

$$\phi = -\frac{2\pi}{\lambda}(2R) = -\frac{4\pi}{\lambda}R \qquad\qquad (2.1)$$

where, 2R represents the round trip distance traversed by the pulse emitted by the SAR with R denoting the slant range and λ represents the wavelength of the radiation. The negative sign accounts for the change in phase of echoes received (Hanssen, 2001).

In other words, during imaging, a decreasing range to a scatterer on the ground results in a positive frequency shift of the echoes received from the target whereas an increasing range to a scatterer results in a negative frequency shift.

It can be inferred from Eq. 2.1, that the propagation phase of a scatterer within a pixel is directly proportional to its slant range distance. However, owing to the periodic nature of the emitted pulse, similar phase values are recorded for all scatterers located at distances of integer multiples of the wavelength from the satellite. Hence, the true phase representing a scatterer is encrypted within the range of phase values representing one whole wavelength of the emitted pulse. In other words the phase is "wrapped" between –π and +π.

The amplitude and phase recorded for a scatterer during SAR data acquisition can be represented as a phasor. A phasor is a vector representation of a complex number where the length of the vector represents the amplitude and the angle describing the vectors orientation represents the phase. The complex phasor representing each element within the cell has components corresponding to backscatter phase and differential path delay phase. The slant-range distance, which defines the differential path delay phase, is measured with respect to a reference surface oriented in a direction normal to the radar look

direction (Rosen et al., 2000). The scattering mechanism of each elemental scatterer contributes to the backscatter phase associated with it (Hanssen, 2001).

2.2.3 SAR Data Resolution

SAR systems resolve objects in two directions, namely the range and the azimuth. The direction perpendicular to the along-track/flight direction and parallel to the radar look direction is called the range. The along-track/flight direction determines the azimuth (Figure 2.1).

Pulse travel times to and from points on the ground are used to resolve their location in the range direction. In addition, range resolution is a function of pulse width or the time period of the pulse. Shorter pulse widths result in increased range resolution. The slant range resolution (Δr) of a SAR can be expressed as:

$$\Delta r = \frac{c\tau}{2},$$ (2.2)

where c is the velocity of light = (3 x 10^8 m/sec) and т is the pulse width. The pulse width is inversely proportional to the radar bandwidth and can be expressed as:

$$\tau = \frac{1}{B},$$ (2.3)

where B is the radar bandwidth. From Eq. 2.2, it is evident that the slant range resolution is independent of the altitude of the satellite during data acquisition. However, shortening of pulse widths results in a decrease in its energy thus affecting the strength of backscatter or amplitude. Therefore, it is not practical to

reduce pulse widths below typical lower-bounds. The procedure of pulse or chirp compression is used to reduce the effective pulse width emitted from an ERS sensor from 37.1 μs to 64 ns, thereby increasing the ground range resolution from 5.5 km to approximately 25 m (Curlander and McDonough, 1991; Hanssen, 2001).

Typically, the ability to resolve any two targets in the azimuth direction depends on the fineness of the beam in the horizontal direction. Conventionally, the locations of any two targets located within the radar beam cannot be resolved by the radar hence limiting the achievable azimuth resolution. SAR systems overcome this limitation by using the Doppler frequency shift principle to resolve the locations of targets even when they are illuminated by the radar beam simultaneously. The resolution in a direction parallel to the motion of the synthetic aperture radar- also referred to as the azimuth, is independent of the altitude of the sensor during imaging and can be expressed as approximately one-half the length of the imaging antenna (Jensen, 2000). As an illustration, the 10-m long antenna mounted on board the ERS-1 makes it possible to achieve an azimuth resolution of ~ 4 m. Azimuth compression is the process adopted in order to realize the full azimuth resolution (Hanssen, 2001).
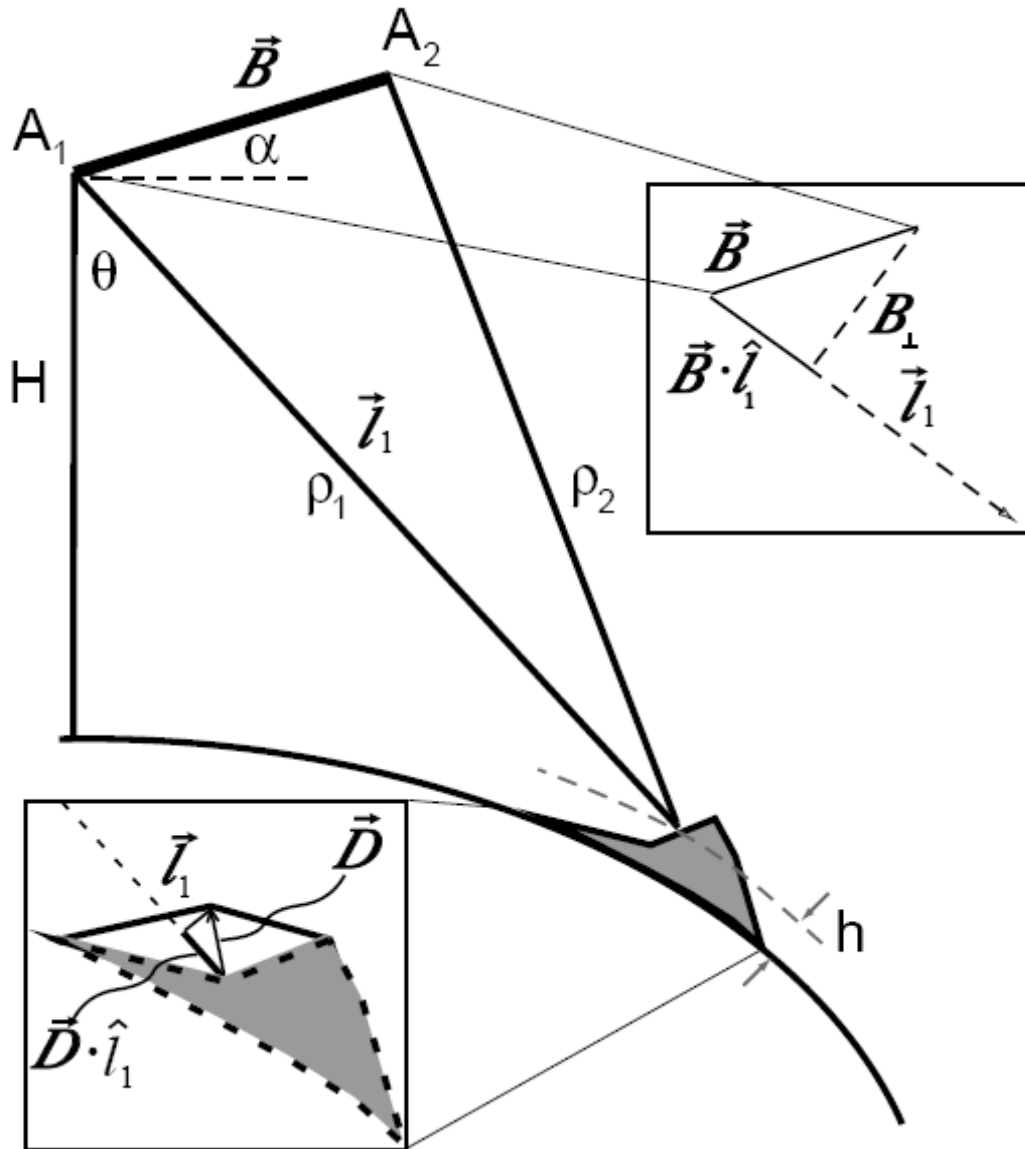
Figure 2.2 Radar viewing geometry in a plane perpendicular to flight track (Burgmann et al., 2000). A_1 and A_2 are the two sensors separated by baseline B. H is the elevation of the reference satellite position from Earth' s surface. ρ_1 and ρ_2 are the slant ranges to the imaged point from sensor positions A_1 and A_2 respectively. θ is the satellite look angle.

2.3 Interferometry

Synthetic aperture radar interferometry (InSAR) is a remote sensing technique that uses differences in line-of-sight distance from slightly different SAR imaging positions to points on the ground to derive high resolution topographic or deformation maps of the imaged area (Burgmann et al., 2000). The applicability of this technique necessitates the availability of at least two synthetic aperture radar (SAR) images of the same area on the ground, acquired from slightly different look angles, are available for analysis. The necessity for at least two acquisitions can be illustrated with the help of Figure 2.3.
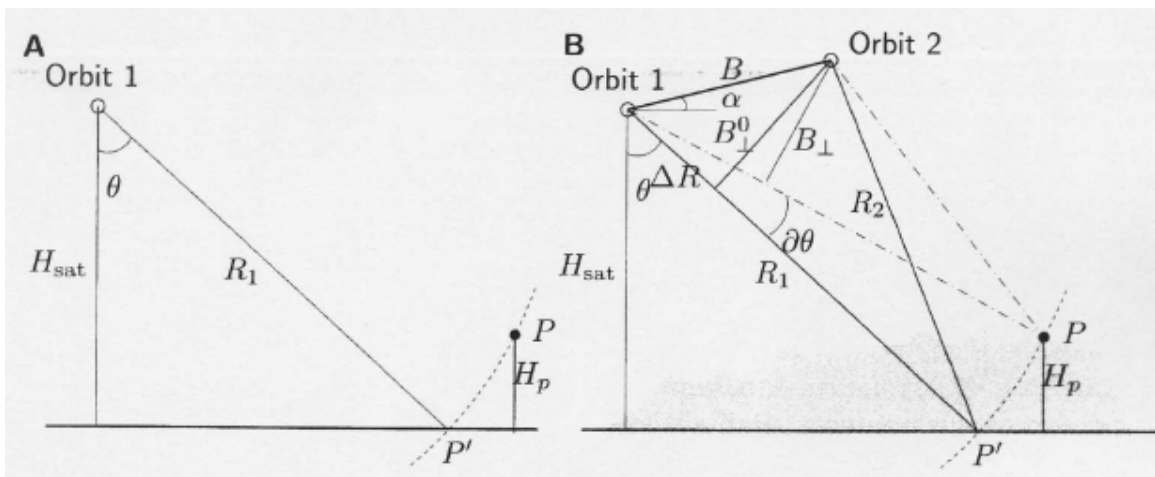
Figure 2.3 (A) Inherent nature of radar to discern objects based only on their range from the radar and the resulting insensitivity to terrain variation. (B) Sensitivity to height variations is obtained by imaging the terrain with two radars separated by a baseline (Hanssen, 2001).

Due to the inherent ranging nature of the imaging radar, a single acquisition gives information relating only to the relative range distance between two targets. Hence, irrespective of their relative angular separation, any two targets located at the same range from the imaging radar are mapped into the same slant range

resolution cell. The image does not provide any information about the angular separation between mapped targets.

However, if the same two targets are imaged from another radar located at a slightly different position in space, it is possible to geometrically relate the elevation difference between the two imaged targets to the spatial separation of the points of acquisition of the two images and the slant range distance of each of the two targets from the two imaging positions. In other words, acquiring imagery from slightly different imaging positions facilitates depth perception (Hanssen, 2001).

The two SAR images may be acquired simultaneously or may be separated in time. Multiplying the complex phasors of all pixels in one acquisition by the conjugate of the complex phasors of all corresponding pixels in the other yields an image known as an interferogram. The complex multiplication on a pixel by pixel basis is equivalent to differencing the phases representing each pixel in both the acquisitions while multiplying their respective amplitudes (Burgmann et al., 2000).

The unwrapped interferometric phase can be represented by the summation of phase contributions from linear deformation ($\phi_{lin-def}$), topography (ϕ_{topo}) and residual phase (ϕ_{res}) as shown in Eq. 2.4. As shown in Eq. 2.5, the residual phase is composed of phase contributions due to *atmospheric path delay* (ϕ_{atm}), non-linear deformation ($\phi_{non-lin-def}$) and *noise* (ϕ_{noise}).

$$\phi_{unw} = \phi_{lin-def} + \phi_{topo} + \phi_{res} \tag{2.4}$$

where,

$$\phi_{res} = \phi_{atm} + \phi_{non-lin-def} + \phi_{noise} \tag{2.5}$$

With reference to the imaging geometry depicted in Figure 2.2, the interferometric phase for the imaged point on the ground derived from acquisitions A1 and A2 can be expressed as:

$$\phi = -\frac{4\pi}{\lambda}(\rho_1 - \rho_2) \tag{2.6}$$

where ρ_1 and ρ_2 represent the slant range distance from satellite positions A_1 and A_2 to the point imaged on the ground.

For baseline (B) values significantly smaller than the slant ranges from the two satellite positions to a target on the ground, the two look vectors can be approximated to be parallel to each other (Zebker and Goldstein, 1986) owing to which Eq.2.6 can be expressed as:

$$\phi = -\frac{4\pi}{\lambda}B\sin(\theta - \alpha), \tag{2.7}$$

where $B\sin(\theta - \alpha)$ denotes $(\rho_1 - \rho_2)$. Physical quantities denoted by all symbols used in Eq. (2.6) and Eq. (2.7) are evident from Figure 2.2. The resolution of an interferogram equals that of the two images used in its derivation.

All pixels in an interferogram representing corresponding ground resolution cells can be represented as complex numbers. As mentioned in Section 2.2.2, the phase representing any imaged target is directly proportional to its slant range distance from the satellite. Two acquisitions being separated in time requires that the same area be imaged during a satellite revisit. This kind of

interferometry is referred to as repeat pass interferometry. It is desired that the repeat orbit be as close as possible to that followed during the initial acquisition. This is, however, not possible in practice thus giving rise to the same area being imaged from two slightly different look angles.

SAR images acquired from slightly different radar look angles have pixels representing the same ground resolution cells with nearly the same backscatter phase but with different path delay phase. During interferogram formation, the common backscatter phase corresponding to the same ground resolution cells is cancelled, thus yielding a phase term that is related to the differential path delay phase. The following sections introduce and discuss important InSAR concepts with emphasis on processing steps and parameters.

2.3.1 Baseline Dependence

The spatial separation between apertures during any two passes for acquisition of the same frame of raw data is known as the baseline between the two acquisitions. The baseline can be represented by the normal baseline and cross-track baseline components or the parallel baseline and perpendicular baseline components (Figure 2.4).

The amount of topographic phase contribution in an interferogram is induced by the difference in slant range distances from the two satellite positions, during image acquisition, to the same point on the ground and depends on the baseline separating the two satellite positions from which the two SAR images used to compute the interferogram were acquired. Greater perpendicular baselines are more sensitive to topographic phase than smaller ones. The

sensitivity of an interferogram to deformation is a function of the wavelength of radiation used for imaging whereas the sensitivity to topography is a function of the perpendicular baseline. The sensitivity to topography can be inferred from the ambiguity height. This quantity defines the topographic elevation change that induces an interferometric phase change of one cycle or 2π radians.
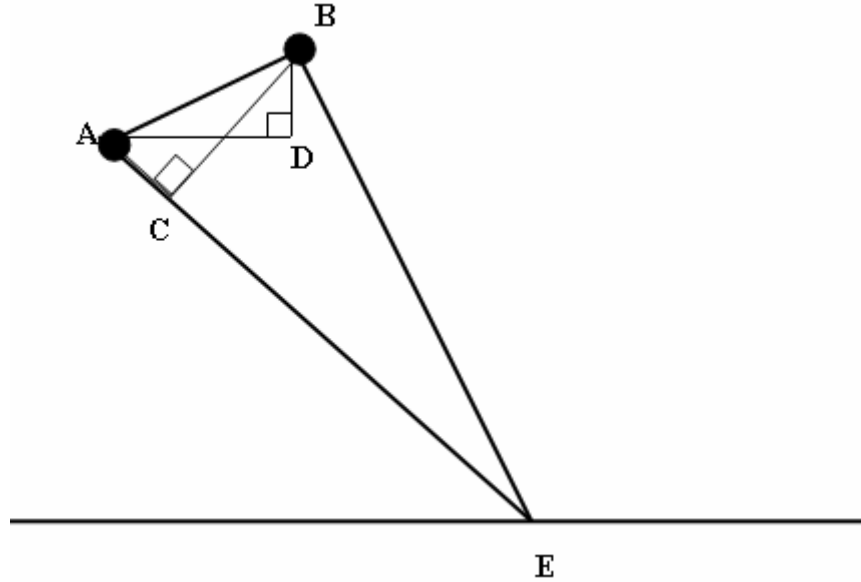
Figure 2.4. Interferometric baseline and its components. AE and BE are the look vectors from satellites A and B to a point E on the ground. BC represents the perpendicular baseline, AC represents the parallel baseline, BD represents the normal baseline and AD represents the across-track baseline.

With reference to the geometry shown in Figure 2.2, the ambiguity height can be expressed as:

$$h_{ambig} = 2\pi \left(\frac{\delta h}{\delta \phi} \right) = \frac{\lambda \rho_1 \sin \theta}{2 B_\perp}, \qquad (2.8)$$

where $\left(\frac{\delta h}{\delta \phi} \right)$ represents the change in topographic height with respect to the interferometric phase, ρ_1 is the slant range distance from the satellite in the

21

reference image, θ is the look angle and $B_\perp$ is the perpendicular baseline (Burgmann et al., 2000). With reference to Figure 2.2, the perpendicular baseline can be expressed as:

$$B_\perp = B\cos(\theta - \alpha),$$ (2.9)

The process of simulating the topographic phase contribution from baseline information and subtraction from the interferogram in order to infer deformation phase is known as Differential Interferometry or DInSAR. The topography defining an imaged area can be obtained from existing Digital Elevation Models (DEM's) for the region in the case of two-pass interferometry or from multiple-pass interferometry. Multiple-pass interferometry consists of using more than two acquisitions such that at least one pair brackets the period when no surface deformation has been recorded. An interferogram calculated between such pairs contains only topographic phase which after simulating and scaling to the baseline defining the pair bracketing the deformation of interest, can be subtracted to obtain a differential interferogram (Rosen et al., 2000).

2.3.2 Deformation Phase

Surface deformation induces a slant range difference that is independent of baseline geometry (Figure 2.2). Owing to the two-way travel time of the transmitted pulse, a surface displacement component equal to one-half the imaging wavelength, measured along the satellite look vector and occurring between two SAR acquisitions, induces one whole phase cycle in the corresponding interferogram. As illustrated in Figure 2.2, a displacement expressed by a vector $\vec{D}$, induces a line-of-sight displacement that can be

expressed by the dot product of the unit vector along the satellite look direction $(\vec{l}_1)$ and $\vec{D}$.

2.3.3 Atmospheric Path Delay Phase

Water vapor in the troposphere increases the travel time of microwave frequency electromagnetic radiation. Thus, the phase value assigned to a point on the ground (given by difference in the phase values recorded at the beginning and end of the two-way transit of microwaves to a point on the ground) that is imaged during such tropospheric conditions will be representative of the slant range distance between the satellite and the point on the ground in addition to atmospheric path delay induced phase difference. The lack of knowledge of tropospheric conditions during image acquisition or the inability to account for such induced path delay, can lead to erroneously considering the entire phase contribution for an imaged point as resulting due only to the slant range distance between the imaged point and the satellite.

The tropospheric condition prevailing at the time of acquisition of a satellite image (SLC), controls whether the image is characterized by atmospheric path delay phase or not. An interferogram calculated using two SLCs with either one characterized by atmospheric path delay, will have phase contributions resulting due to atmospheric path delay. On the other hand, an interferogram calculated between two SLCs acquired during exactly similar tropospheric conditions will not contain atmospheric path delay phase.

2.4 InSAR Processing Flow

The flow chart in Figure 2.5 illustrates the sequential order of steps involved in differential interferometry. A detailed description of each of the steps mentioned in the flowchart above follows.

2.4.1 Offset Estimation and Coregistration

Acquisition of SAR data from two satellite geometries to facilitate depth perception results in a relative shift or offset in the positioning of pixels between two SAR images used for interferometry. The shift between images in the range direction is a function of the baseline separating the two imaging geometries, whereas, a relative shift in the azimuth direction results owing to differing relative times of imaging the same area during the two data takes (Hanssen, 2001). The relative shift between the images results in the same ground resolution cell being assigned different pixel locations in the two images.

```
┌─────────────────┐          ┌─────────────────┐
│   MASTER SLC    │          │    SLAVE SLC    │
└─────────────────┘          └─────────────────┘
         │                            │
         └──────────────┬─────────────┘
                        ▼
            ┌───────────────────────┐
            │   OFFSET ESTIMATION   │
            └───────────────────────┘
                        │
                        ▼
            ┌───────────────────────┐
            │    COREGISTRATION     │
            │    & RESAMPLING       │
            └───────────────────────┘
                        │
                        ▼
            ┌───────────────────────┐
            │    INTERFEROGRAM      │
            │     CALCULATION       │
            └───────────────────────┘
                        │
                        ▼
         ┌─────────────────────────────┐
         │  PRELIMINARY BASELINE       │
         │       ESTIMATION            │
         └─────────────────────────────┘
                        │
                        ▼
        ┌───────────────────────────────┐
        │  TOPOGRAPHY AND EARTH         │
        │  CURVATURE PHASE SUBTRACTION  │
        └───────────────────────────────┘
                        │
                        ▼
            ┌───────────────────────┐
            │   PHASE UNWRAPPING     │
            └───────────────────────┘
                        │
                        ▼
      ┌─────────────────┐      ┌─────────────────────────────┐
      │   BASELINE      │─────▶│  DIFFERENTIAL INTERFEROGRAM │
      │  IMPROVEMENT    │      │        GENERATION           │
      └─────────────────┘      └─────────────────────────────┘
```
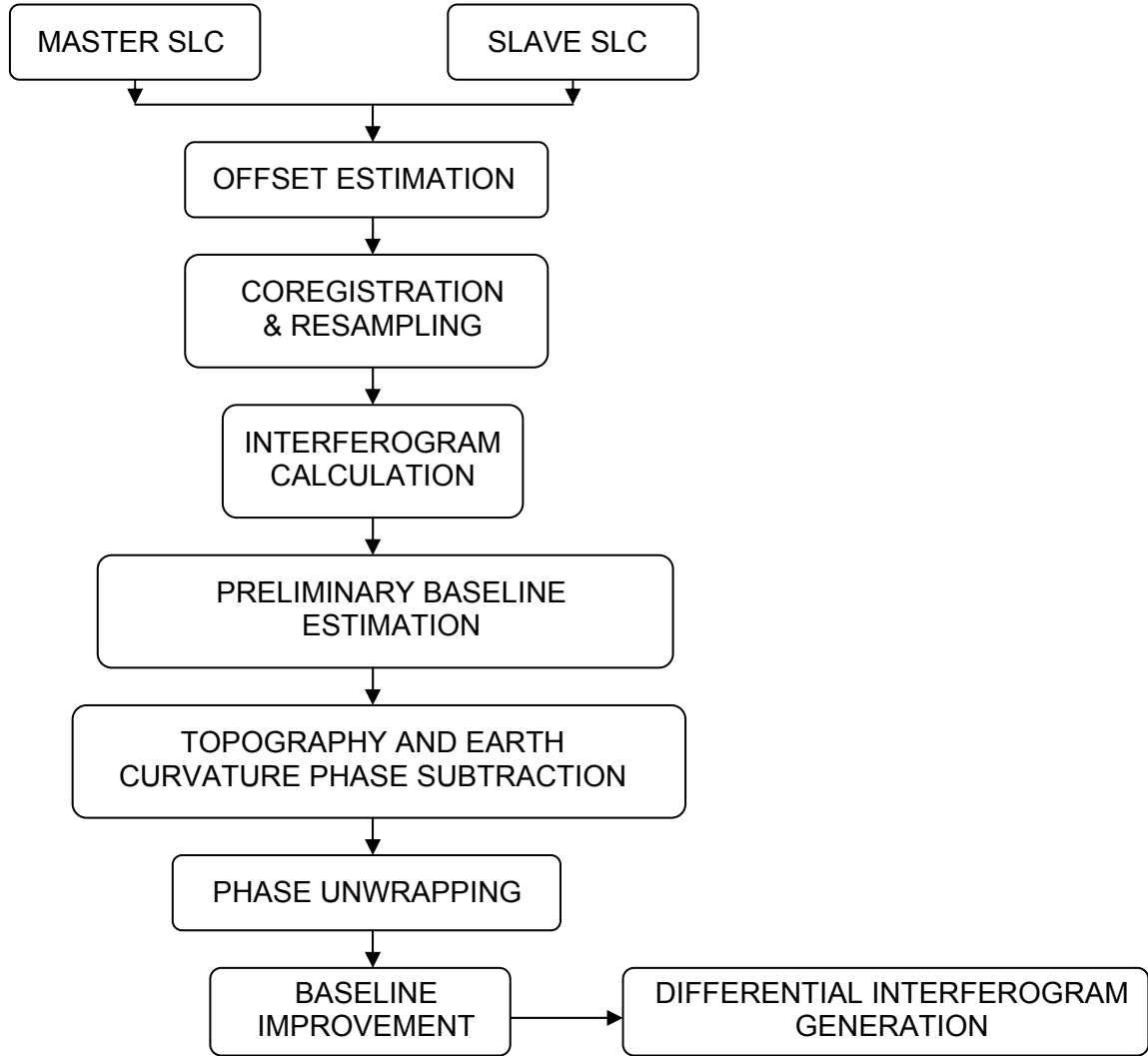
Figure 2.5. Main steps for DInSAR

Coregistration is the process of aligning the pixels corresponding to the same ground resolution cell in two different SAR images. The two SAR images used for interferogram calculation must be coregistered in order to ensure that phases corresponding only to those pixels, in the two SAR images, that represent the same ground resolution cell are used for interferometric calculations. Sub-pixel accuracies ranging from $1/8^{th}$ to $1/10^{th}$ of a pixel are

recommended for obtaining reliable elevation estimates. Usually, one of the image geometries is chosen as the reference for coregistration. The reference image is also referred to as the master, whereas the image(s) being coregistered into the reference geometry is referred to as the slave.

Owing to different imaging geometries, similar areas on the ground are represented in slightly shifted grids representing the different SAR images although the grid spacing in both images remains the same. Hence a ground resolution cell contributing to a single pixel in the slave may be contributing only to a part of a pixel in the master. In order to be able to perform interferometric calculations, the complex phase values of the slave image need to be calculated for the pixel locations of the master as implied by the coregistration coefficients.

As mentioned in Hanssen and Bamler (1999), the phase values at the new pixel locations can be obtained by reconstructing the continuous phase field from the sampled data corresponding to the slave and then resampling the reconstructed phase field at the inherent sampling rate of the master.

2.4.2 Interferogram Calculation

Image coregistration and resampling is followed by interferogram calculation. As mentioned in Section 2.3, an interferogram is computed on a pixel-by-pixel basis by multiplying the complex phasor of a pixel in the master by the complex conjugate of the corresponding pixel in the slave. Corresponding pixels are those that represent the complex contribution from the same ground resolution cell. Hence, accurate coregistration is critical in ensuring accurate

interferogram calculation. Following the notation used in Hanssen (2001), interferogram calculation can be expressed as:

$$y_1 y_2^* = |y_1| \exp(j\psi_1)|y_2| \exp(-j\psi_2) = |y_1||y_2| \exp(j(\psi_1 - \psi_2)), \qquad (2.10)$$

where y_1 and y_2 depict the complex phasors of corresponding pixels in both the images used in interferogram calculation, y_2^* depicts the conjugate of the complex phasor for the pixel in the slave image, whereas ψ_1 and ψ_2 represent the phase of corresponding pixels in the master and slave images.

2.4.3 Baseline Estimation

In deformation mapping applications, accuracy in simulating the phase contribution from topography and the curvature of the earth dictate the accuracy in the relative deformation estimated using differential interferometry. When the phase contribution due to earth curvature is subtracted from an interferogram, the resulting phase image contains phase contributions due only to the topography of the imaged area and any deformation bracketed by the two images used in interferogram calculation. This operation of subtracting earth curvature phase contribution is known as interferogram flattening. Accuracy in these operations is dictated by the accuracy of baseline estimation.

During the course of a satellite orbit, the spatial location of the satellite is expressed in the form of state vectors which constrain the satellite location in terms of position, velocity and time. The state vectors are determined from satellite tracking data, gravity models and estimated atmospheric drag effects from dynamic models (Hanssen, 2001). Several algorithms have been proposed

for accurate interferometric baseline estimation (e.g., Goyal and Verma, 1995 and Fang et al., 2004)

2.4.4 Phase Unwrapping

As explained in Section 2.2.2, a complex interferogram represents differential path delay phase for each pixel by phase values wrapped in the range (-π, π). Determination of the absolute phase value for these pixels entails the addition of an integer number of whole cycles of phase or integer multiples of 2π radians to the complex phase of each pixel. The absolute phase representing the displacement or range change for each pixel is determined in two steps.

The first step is performed to find the integer number of whole cycles that need to be added in order to achieve the correct relative phase difference of all pixels relative to a reference pixel. This procedure is known as phase unwrapping. Once the complex phase of all pixels has been unwrapped with respect to the phase of a reference point in the interferogram, the absolute unwrapped phase determination step consists of determining the constant multiple of 2π that should be added to the relative phase of all pixels as determined from the phase unwrapping step (Rosen at al., 2000).

Inherent fringe gradients, expressed in phase cycles per pixel, dictate the difficulty in unwrapping an interferogram correctly. High fringe gradients increase the difficulty in phase unwrapping. Fringe gradients in an interferogram depend on three main parameters, namely:

1. Perpendicular baseline,
2. Terrain slope with respect to look vector, and

3. Wavelength used for imagery (Rosen et al., 2000).

Fringe gradients increase with increase in baselines. Terrains sloping toward the sensor induce greater fringe gradients than those sloping away. Fringe gradients are inversely proportional to wavelength with short wavelengths yielding high fringe gradients. As mentioned in Gens (2003), most of the techniques proposed to accomplish phase unwrapping can be broadly classified under two methods, namely:

1. Path following methods, and

2. Minimum norm methods.

Path following methods operate by identifying and delineating branch cuts and restricting the unwrapping direction to regions bounded by them. Branch cuts delineate zones characterized by smoothly varying phase fields which can be unwrapped using the traditional assumptions.

As mentioned in Gens (2003), the branch-cut algorithm (Goldstein, et al., 1988), Flynn's minimum discontinuity algorithm (Flynn, 1997), minimum cost flow networks (Constantini, 1998) and minimum spanning tree algorithm (Chen and Zebker 2000) are some path following methods proposed to achieve two dimensional phase unwrapping.

Minimum-norm methods solve the problem mathematically and achieve unwrapping by solving for the integer multiples of 2π that mimimize the difference between the wrapped and unwrapped phase gradients in the range and azimuth directions (Gens, 2003; Feretti et al., 2007). More details on the topic can be found in Ghiglia and Pritt (1998).
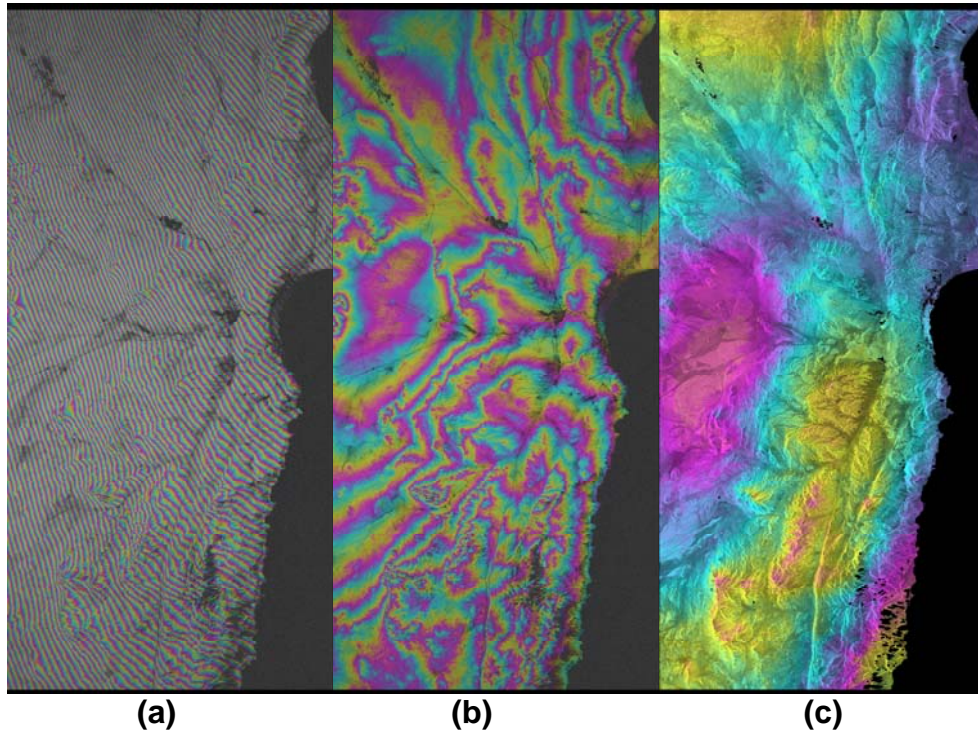
Figure 2.6 (a) Interferogram between March 1996 ERS1 and March 2000 ERS2 acquisitions over Mejillones peninsula, (b) the interferogram with earth curvature removed and (c) the unwrapped differential interferogram. The acquisitions are separated by a 20 m baseline. All figures above are in descending satellite look geometry.

2.4.5 Preprocessing for Unwrapping

Preprocessing involves steps to reduce phase noise and phase complexity to aid in phase unwrapping. Multi-looking and filtering are two commonly adopted preprocessing steps.

Multi-looking is a process by which phase values of a specified number of interferogram pixels are averaged in order to reduce noise (Hanssen, 2001). Multi-looking results in loss of resolution which can be disadvantageous when applied to interferograms with high fringe gradients. However, multi-looking can be effectively applied to datasets with smooth phase fields and low fringe

gradients. In addition, multi-looking helps reduce processing time by reducing data set sizes.

Filtering on the other hand, aids in reducing phase noise while maintaining the data set resolution. Care should be taken while adopting filter parameters in order to avoid generation of filtering artifacts in regions of non-uniform phase fields or loss of whole phase cycles owing to over filtering. Both these effects induce errors during phase unwrapping.

3. RESULTS AND DISCUSSION

3.1 Introduction

The findings of this study have been presented in four parts in this chapter. In the first part, the co-seismic crustal deformation fields corresponding to the 2000 and 2002 earthquakes as obtained from InSAR processing are presented. The second part introduces forward modeling methods that were adopted to derive parameters describing fault segments that ruptured during the events considered in this study. Details about the Coulomb failure criterion and how it was used to infer stress redistribution resulting from the earthquakes have been presented in the third section. A detailed discussion of the results and the conclusions of the study are presented in the final part.

3.2 Co-seismic Deformation from InSAR

SAR data acquired over the study area and bracketing the dates of occurrence of the 2000 and 2002 earthquakes were used to compute the corresponding co-seismic interferograms. The details of SAR data used for interferometric computations are shown in Table 3.1.

Table 3.1 Details of SAR acquisitions used for interferometry

Event Date	SAR Platform	Track	Frame	Orbit	Date
15-Dec-00	ERS-2	250	2835	24152	3-Dec-99
	ERS-2	250	2835	29663	22-Dec-00
	ERS-2	250	2835	27659	4-Aug-00
3-Feb-02	ERS-2	250	2835	32669	20-Jul-01
	ERS-2	250	2835	38180	9-Aug-02

Figure 3.1 and Figure 3.2 show the co-seismic differential interferogram and the corresponding satellite line of sight displacement fields as computed for the 2000 and 2002 events. The satellite look direction that was adopted to acquire the master and slave SAR data used in differential interferogram calculation have been depicted by a bold arrow in Figure 3.1. As can be seen from Figure 3.1, two phase anomalies are evident in the co-seismic differential interferogram defining the 2000 event. The smaller of the two anomalies, marked as Event 1 in Figure 3.1, is reported to have occurred approximately 15 seconds before Event 2 which corresponds to the bigger of the two phase anomalies. Event 1 has been associated with an M_w 5.1. Irregularities associated with both the co-seismic phase anomalies correlate spatially with the Eber and Aksehir Lakes situated in the Aksehir-Afyon graben. Figure 3.2 shows the coseismic interferogram and the satellite line of sight displacement map corresponding to the February 3rd, 2002 earthquake. The phase anomaly due to the earthquake is marked by the black box in the figure. As is evident from the figure, the differential interferogram contains phase contribution from more sources than just deformation. The availability of just two SAR scenes bracketing the earthquake limited the quality of the co-seismic deformation field computed from the pair. The high fringe gradient resulting from the co-seismic crustal deformation corresponding to this event necessitated that the differential interferogram shown in the figure be scaled such that one color cycle represents two cycles of phase.
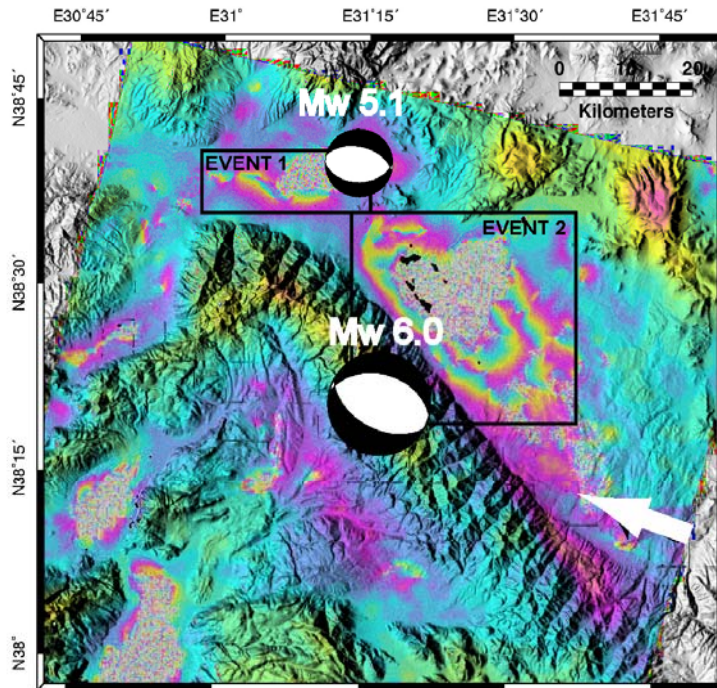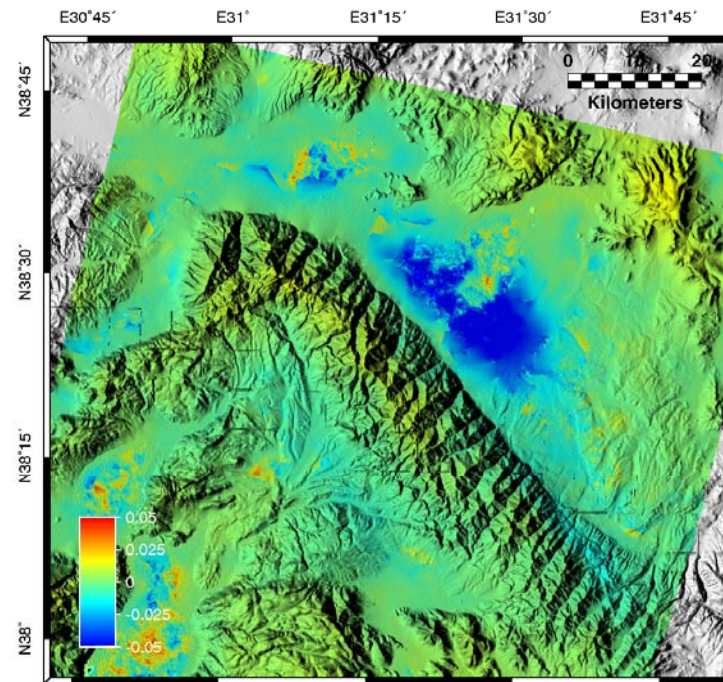
Figure 3.1 (a) Differential interferogram for 15th December 2000 earthquakes-one color cycle denotes 2π radians of phase and equals 28 mm of range change, (b) corresponding satellite line-of-sight displacement field. White arrow depicts satellite look direction.

Figure 3.2 (a) Differential interferogram for 3rd February 2002 earthquakes-one color cycle denotes 4π radians of phase and equals 56 mm of range change, (b) corresponding satellite line-of-sight displacement field. White arrow depicts satellite look direction.
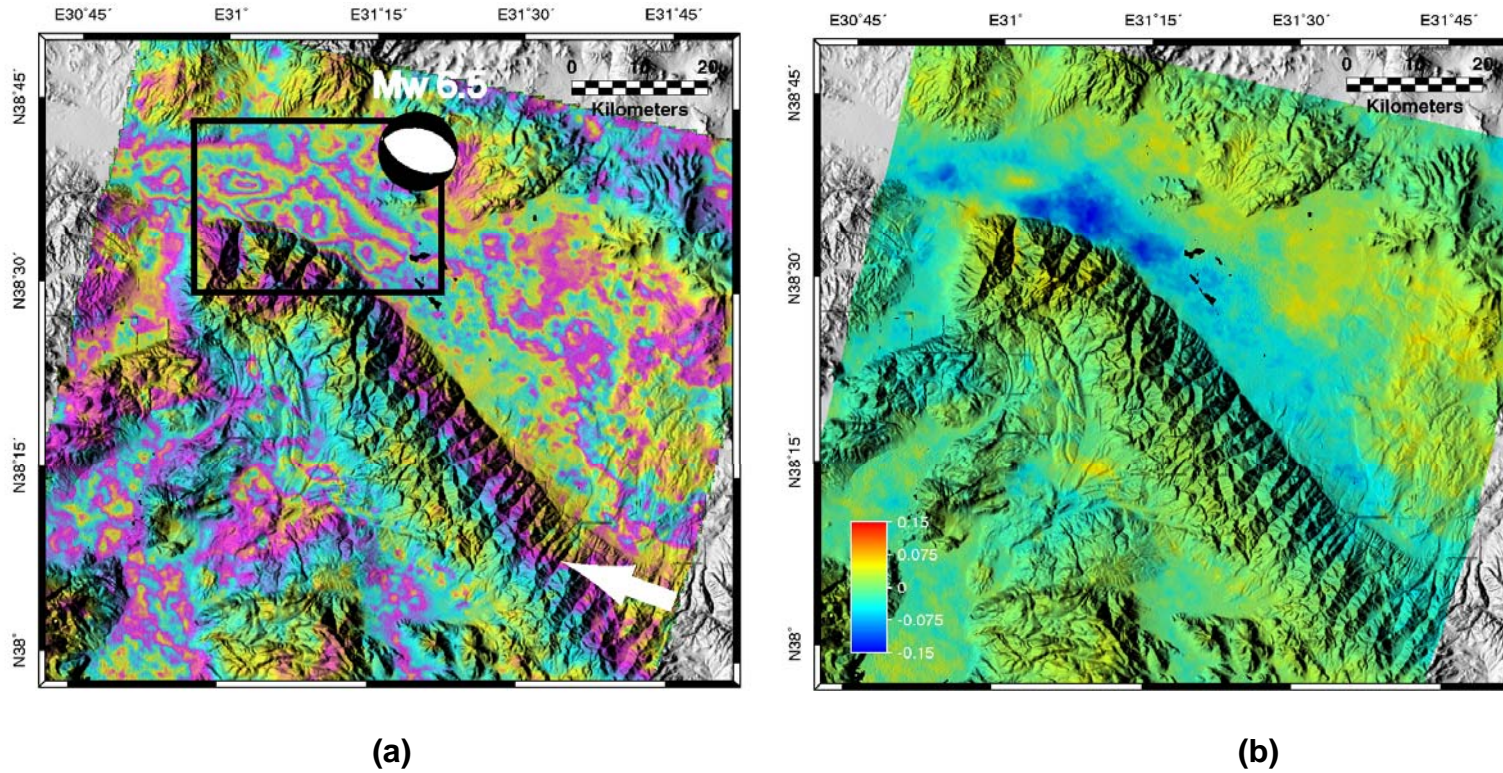
Crustal subsidence as inferred from the co-seismic displacement fields corresponding to all events, is consistent with what would be associated with normal faulting events in the prevalent regional extensional regime.

3.3 Elastic Dislocation Modeling

Parameters describing fault patches that ruptured during the 2000 and 2002 events were modeled using the program RNGCHN (Feigl and Dupre', 1999). The program uses Okada's dislocation formulation (1985) to calculate a component of crustal displacement resulting from dislocation on a fault patch at depth assuming that the fault in situated in an elastic half-space. A trial and error method was adopted to obtain the fault parameters that produced a line of sight displacement field that was comparable with the co-seismic deformation field computed using InSAR. Hence, in effect the fault parameters were derived by forward modeling.

Estimates of the following fault patch parameters were obtained by adopting the trial and error method:

1 Dimensions (Length and Width),

2 Strike and dip,

3 Depth, and

4 Amount of slip on the patch.

Figure 3.3 and Figure 3.4 compare the observed phase associated with the line-of-sight component of the displacement resulting from the corresponding events with the displacement phase field modeled using RNGCHN. The presence of phase contribution from sources other than co-seismic deformation in the

differential interferogram representing the 2002 event must be noted in the context of related uncertainties that can be associated with the modeled fault parameters. The modeled fault patch parameters, as computed for the 2000 and 2002 events are shown in Table 3.2.

As can be seen from Table 3.2, the bottom left of the fault patch that was modeled to have ruptured during the M_w 6.0 December 15th, 2000 earthquake was situated at a depth of 12 km and the modeled fault patch was associated with a dip of 45°. On the other hand, the February 3rd, 2002 event was modeled to have ruptured a fault patch whose bottom was located at 8 km while the patch itself was associated with a dip of 60°.

Hence, the two events were assumed to have occurred on a listric faulting Sultandagi Aksehir fault. The listric geometry was modeled as two sections-(a) a section dipping at 60° between the surface and a depth of 8 km and (b) a section dipping at 45° between depths of 8 km and 12 km.
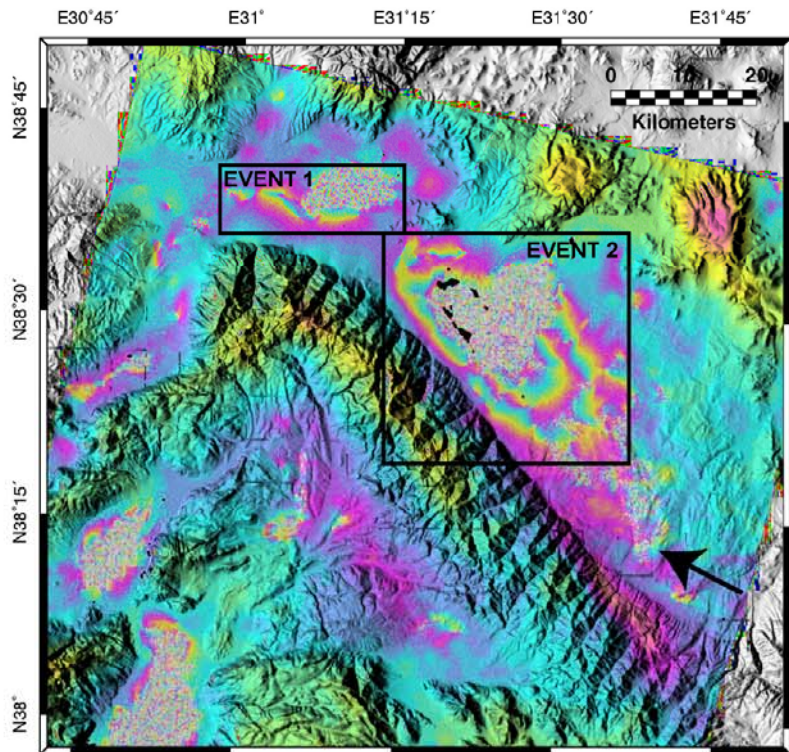
(a)
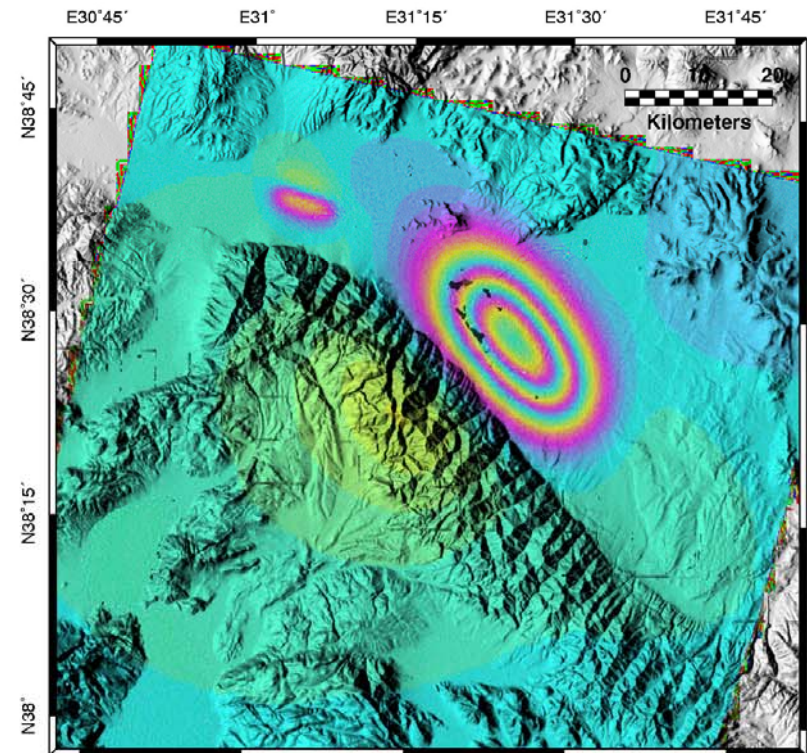
(b)

Figure 3.3 (a) Differential interferogram for 15th December 2000 earthquakes, (b) differential interferogram corresponding to fault parameters modeled using RNGCHN. One color cycle denotes 2π radians of phase and equals 28 mm of range change in both figures.
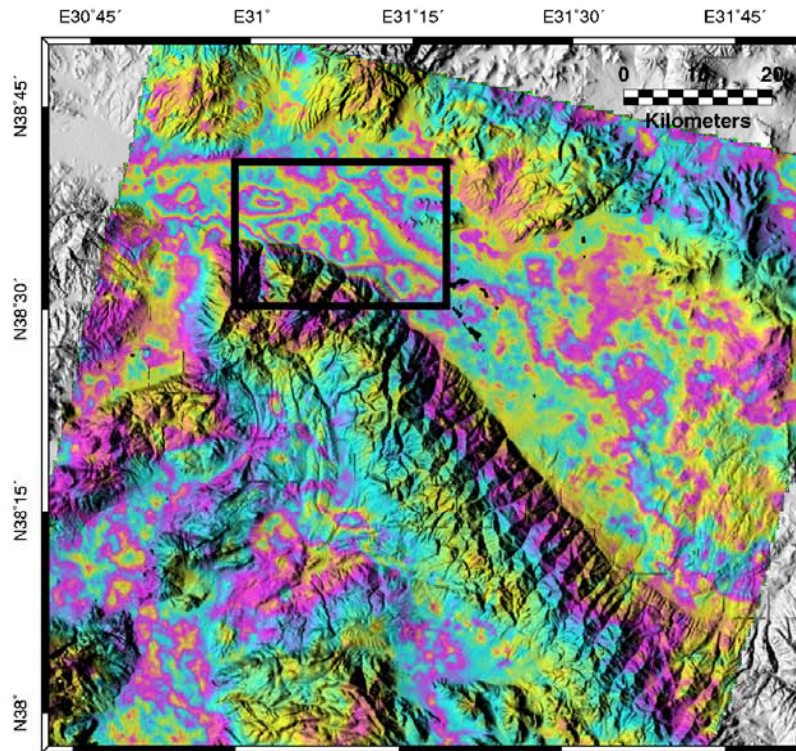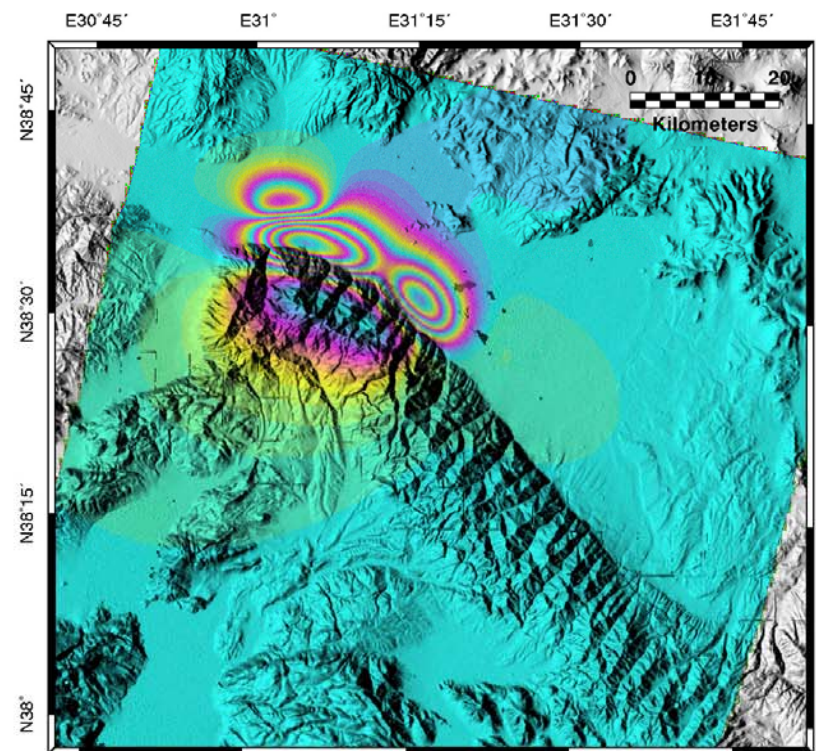
Figure 3.4 (a) Differential interferogram for 3rd February 2002 earthquake, (b) differential interferogram corresponding to fault parameters modeled using RNGCHN. One color cycle denotes 4π radians of phase and equals 56 mm of range change in both figures.

Table 3.2 Fault parameters modeled using RNGCHN. Easting and Northing are with respect to NUTM 36.

| Event (Year, Mw) | Bottom Left of Fault Patch | | | Length (km) | Width (km) | Strike (°) | Dip (°) | Slip | | Geodetic M_o (Nm) | Geodetic M_w (Nm) |
	Easting (km)	Northing (km)	Depth (km)					Dip (mm)	Strike (mm)		
2000 (Mw 5.1)	331.5	4279.7	3.4	8	2	110	70	120	60	6.44E+16	5.21
2000(Mw 6.0)	373.6	4251.9	11.9	20	5	320	45	650	-	1.95E+18	6.19
2002 (Mw 6.5)	345.0	4271.1	8	14	5	285	60	500	-	1.73E+18	6.16
	355.4	4262.1	8	9	5	315	60	500	-		

The moment magnitude calculated from the modeled fault parameters is shown in Table 3.2. All of the modeled fault parameters should be considered in the context of the tradeoff between the depth of source versus slip magnitude and down-dip width. For example, a shallower source would require a wider down dip width and a smaller magnitude of slip in order to match the same fringe pattern.

The fault parameters for the two 2000 events can be associated with a moment magnitude that is consistent with the reported seismic moment. However, a comparison of the seismic and geodetic moment magnitudes for the 2002 event yields that the modeled fault parameters under-estimate the moment (and moment magnitude). One of the several possible reasons for the discrepancy between the observed and the modeled moments associated with the February 3rd, 2002 earthquake can be the noisy nature of the InSAR displacement map that was available for modeling the fault parameters.

3.4 Coulomb Failure Criterion

Observed correlation between main shock and after shock locations and, in some cases, future main shock locations, has been explained by means of static Coulomb stress changes occurring on fault segments in the vicinity of the main shock. Specifically, with respect to thrust faulting environments, the 1983 Coalinga earthquake (M_w 6.7) has been shown to increase Coulomb stress in regions around the locations of 1983 Nunez earthquake (M_w 6.0) by 10 bars and 1985 Kettleman Hills earthquake (M_w 6.0) by 1 bar respectively.

Similarly, locations where Coulomb stress increases were calculated to range between 2 and 20 bars and resulting from the 1960 (M_w 9.5) and 1995 (M_w 8.1) earthquakes in Chile have been shown to correlate with locations of after shocks following both the events. With respect to strike-slip environments, the 1857 Fort Tejon (M_w 7.9) earthquake has been shown to have increased Coulomb stress on the Coalinga fault by 1 bar while causing a decrease in the Coulomb stress on the Coast Ranges thrust faults (Lin and Stein, 2004).

Static stress changes on faults in the study area resulting from redistribution of stresses released due to the December 2000 and February 2002 main shocks were assessed using the Coulomb failure criterion. The Coulomb failure criterion can be represented as,

$$\Delta\sigma_f = \Delta\tau_s + \mu'\Delta\sigma_n \tag{3.1}$$

where, $\Delta\sigma_f$ represents the change in static coulomb stress on the receiver faults, $\Delta\tau_s$ represents the change in shear stress on the receiver faults and $\Delta\sigma_n$ represents the change in the normal stress on the receiver faults. μ' represents the effective coefficient of friction of the receiver fault (King et al., 1994).

Coulomb stress calculation for faults in the study area were performed using Coulomb 3.0. In conformation with the notation used in Coulomb 3.0, segments of the SAF that slipped during the two main shocks were considered as source faults whereas faults on which the resulting static coulomb stress changes were calculated were considered as receiver faults.

3.5 Results

Figure 3.5 shows the Coulomb stress change resulting from each of the events and the resulting cumulative coulomb stress change. The figure shows coulomb stress changes calculated at a depth of 5 km on all fault planes oriented at a strike of 300° and dipping at 60°. The fault segments have been labeled A through F in Figure 3.5b which is intended to geographically reference the coulomb stress change maps. Fault segment F on Figure 3.5 b represents the segment which ruptured during the smaller of the two December 15th, 2000 events. Segment D represents the segment that ruptured during the Mw 6.0 December 15th, 2000 earthquake whereas segment B and C were modeled to have ruptured during the Mw 6.5 February 3rd, 2002 earthquake.

To complement Figure 3.5, coulomb stress changes resulting from all three earthquakes have been plotted as a function of depth in Figure 3.6 through Figure 3.8. Coulomb stress changes are shown for profiles running through the center of fault segments that were subjected to static coulomb stress changes as a result of each of the three earthquakes.
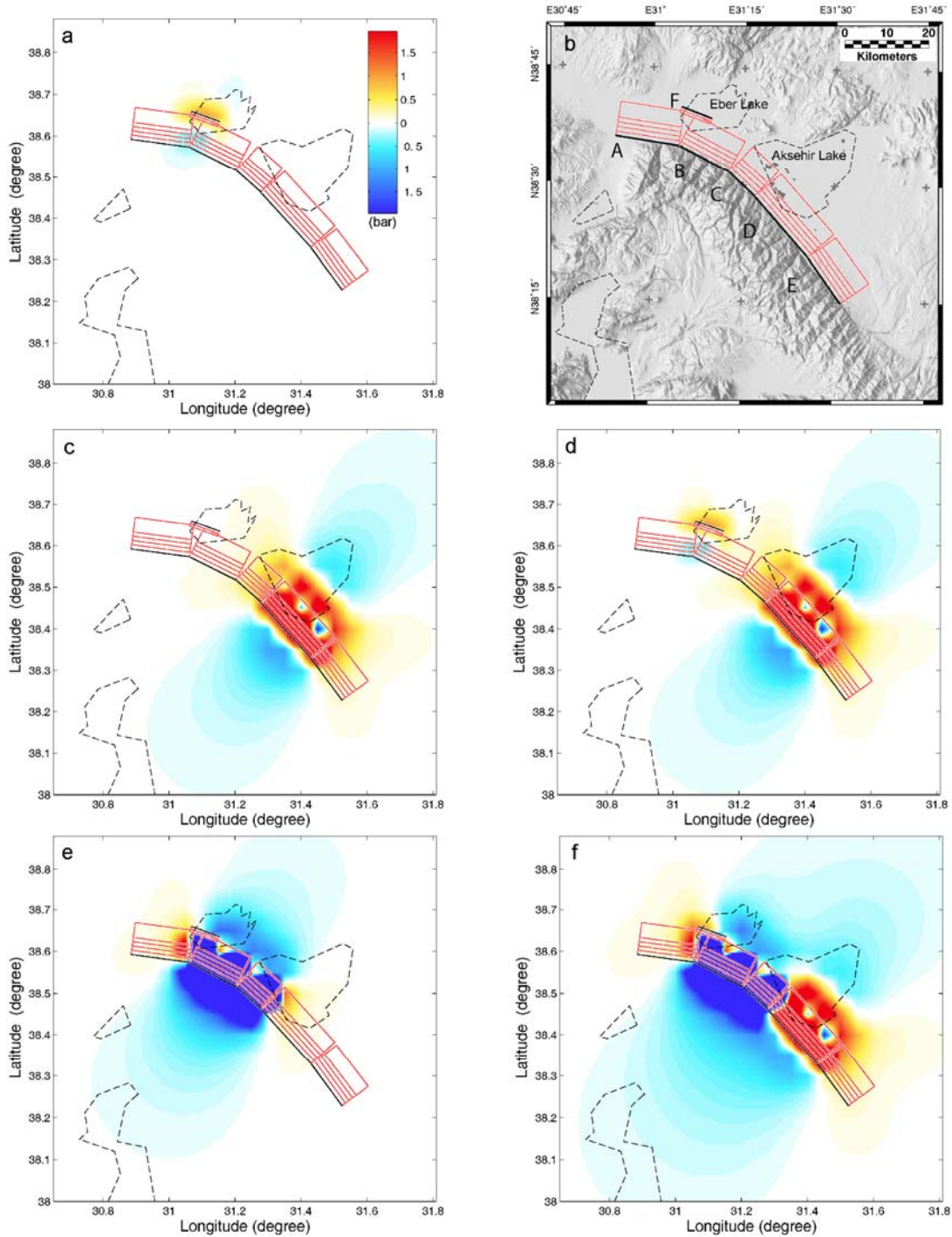
Figure 3.5 Coulomb stress changes resulting from (a) M_w 5.1 December 15th, 2000 event, (c) M_w 6.0 December 15th, 2000 event, (e) M_w 6.5 February 3rd, 2002 event, (d) cumulative coulomb stress change due to the two December 15th, 2000 events, (f) cumulative coulomb stress change due to all 2000-2002 events. All stress changes shown in maps were calculated at a depth of 5 km. The scale bar shown in (a) applies to all maps in this figure. On the scale bar, red denotes an increase in Coulomb stress whereas blue denotes a decrease.

As can be seen from Figure 3.6, although the coulomb stress redistribution resulting from the smaller of the 2000 event's did not result in a coulomb stress increase on fault segment D that ruptured during the bigger of the two 2000 events, it did result in a decrease in coulomb stress on the fault segment A which did not rupture in 2002. Given that the rupture during the February 2002 earthquake was modeled to have ruptured segments C and D between depths of 4 km and 8 km from the surface, it could be expected that any propagation in the rupture would occur at similar depths on adjacent segments.

Additionally, Figure 3.7 indicates that the rupture of segment D between depths of 8 km and 12 km from the surface during the M_w 6.0 December 2000 earthquake, resulted in an increase in static coulomb stress on the segments C, D and E at a depth of 5 km. Strain release during the earthquake corresponds with the zone of coulomb stress decrease between depths of 8 km and 12 km in Figure 3.7d. The depth of coulomb stress increase along segment C correlates with the depth range at which the fault patch corresponding to the 2002 earthquake was modeled to have ruptured. Also evident from Figure 3.7c and Figure 3.7e is that the M_w 6.0 December 2000 earthquake resulted in an increase in static coulomb stress along the entire listric cross-section of segments C and E.

Figure 3.6 Coulomb stress changes due to M$_w$ 5.1 December 15th, 2000 event. (a) Stress change at 5 km depth, (b) stress change with depth along profile A-A', (c) stress change with depth along profile B-B'. On the scale bar, red denotes an increase in Coulomb stress whereas blue denotes a decrease.
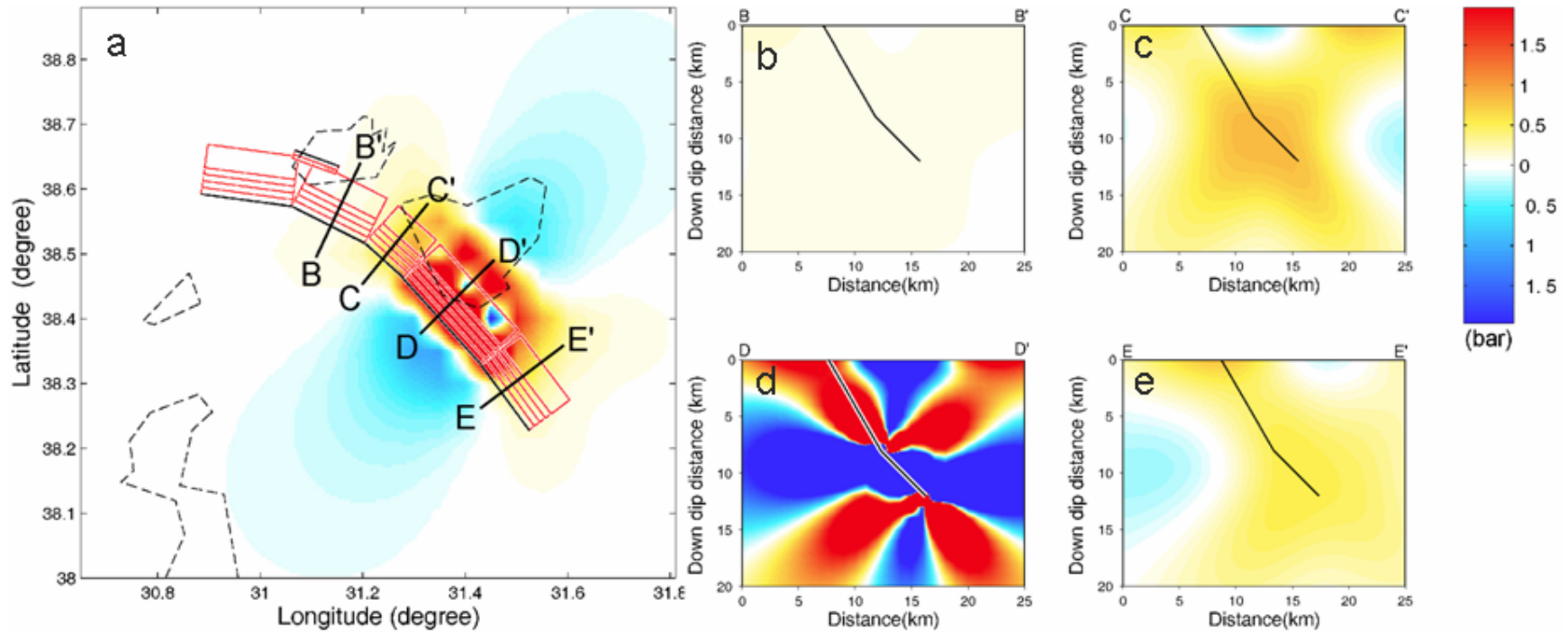
Figure 3.7 Coulomb stress changes due to M_w 6.0 December 15th, 2000 event. (a) Stress change at 5 km depth, (b)stress change with depth along profile B-B',(c)stress change with depth along profile C-C',(d) stress change with depth along profile D-D',(e) stress change with depth along profile E-E. On the scale bar, red denotes an increase in Coulomb stress whereas blue denotes a decrease.

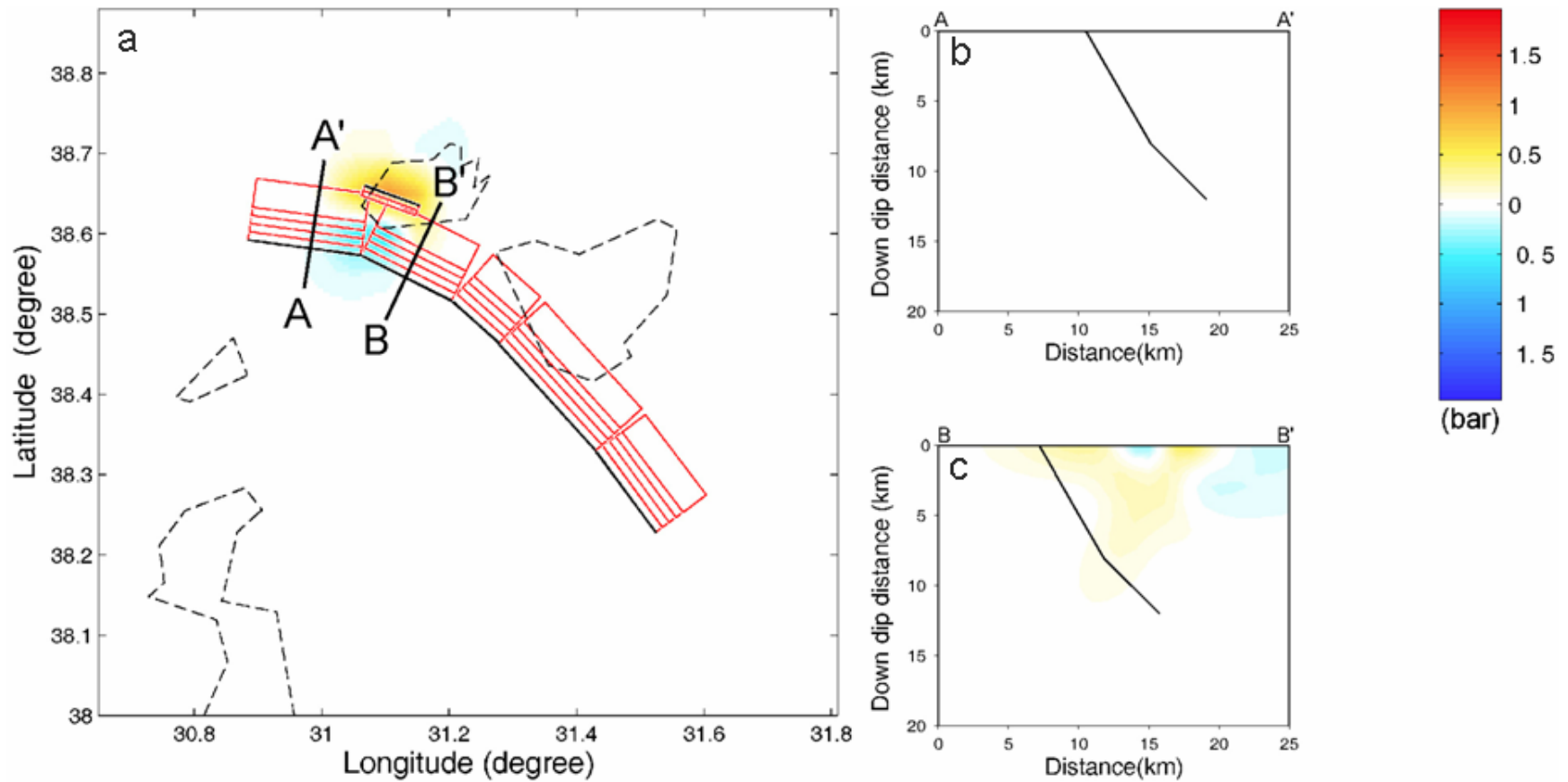**Figure 3.8** Coulomb stress changes due to M_w 6.5 February 3rd, 2002 event. (a) Stress change at 5 km depth, (b) stress change with depth along profile A-A',(c)stress change with depth along profile B-B',(d) stress change with depth along profile C-C',(e) stress change with depth along profile D-D' On the scale bar, red denotes an increase in Coulomb stress whereas blue denotes a decrease.
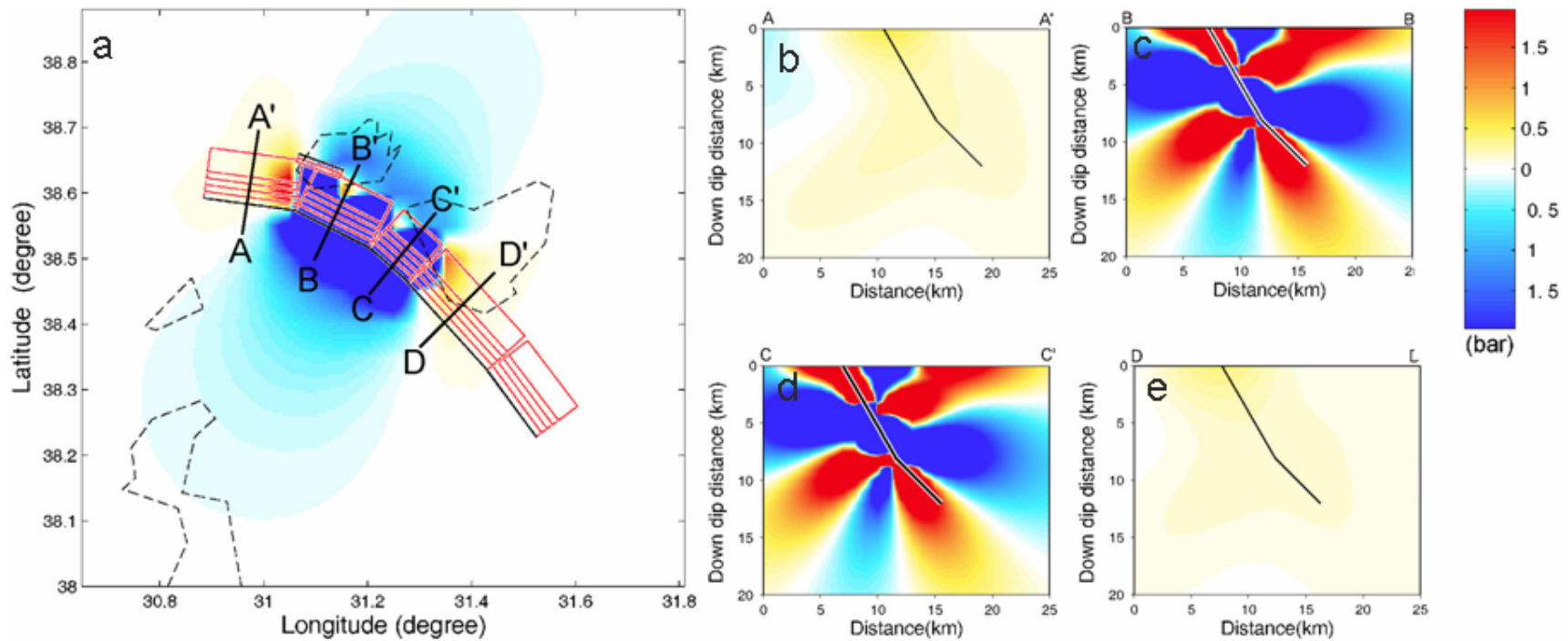
Figure 3.8a shows that while the rupture during the M_w 6.5 February 2002 earthquake decreased coulomb stress across the Aksehir-Afyon graben at a depth of 5 km, segments A and D were subjected to an increase in static coulomb stress at a similar depth. Considering that the M_w 6.0 2000 earthquake increased coulomb stress up to depths of 8 km on segment D, the increase in coulomb stress at similar depths as shown in Figure 3.8e would mean that the shallower section of segment D has undergone a net increase in coulomb stress as a result of the 2000 and 2002 events. On the other hand, comparing Figure 3.7a and Figure 3.8b shows that coulomb stress increase on segment A was not initiated until the occurrence of the M_w 6.5 February 2002 event.

3.6 Implications for Earthquake Hazard

The results of this study have direct implications for understanding the earthquake hazard in Southern Turkey. Specifically, questions regarding the effect of Coulomb stress changes on regional seismic hazard can be addressed.

Zones of Coulomb stress increase induced by the February 3rd,2002 earthquake were observed to be located in close proximity to highly populated (in excess of 100,000) cities like Afyon and Aksehir, besides other less populated but inhabited dwellings around Lake Eber and Lake Aksehir. Results also show Coulomb stress increases on parts of the fault located immediately above the ruptured segments, which is indicative of increased seismic activity in such regions. Cumulative stress change computations reveal a general reduction in Coulomb stress across the Aksehir-Afyon graben as a result of the 2000-2002 events, which is indicative of reduced seismic activity.

However, it is imperative that these inferences be considered in conjunction with the uncertainties associated with the modeled fault parameters used in Coulomb stress change computations. Better constraints on the fault model and the consideration of existing regional strain fields for Coulomb stress change computations will help provide a realistic assessment of imminent hazard. Despite deficiencies, these results can assist outline considerations that need further investigation.

3.7 Conclusions

Analysis of static coulomb stress redistribution resulting from the December 15th, 2000 earthquakes and the February 3rd, 2002 earthquake on a listric fault geometry model of the Sultandagi Aksehir fault suggests the following:

1. The M_w 5.1 December 15th, 2000 earthquake resulted in a decrease in coulomb stress on the Sultandagi Aksehir fault segment which did not rupture in 2002 and hence could be the reason for the extent of rupture associated with the February 2002 earthquake .

2. The M_w 6.0 December 2000 earthquake resulted in an increase in static coulomb stress on the immediately adjacent fault segments. One of these adjacent segments ruptured during the M_w 6.5, February 2002 earthquakes. This suggests that the December 2000 earthquake triggered the rupture of the Sultandagi Aksehir fault segment associated with the February 3rd 2002 event.

3. The cumulative coulomb stress changes resulting from all earthquakes analyzed in this study indicates a net increase in coulomb stress change along the cross section of the fault up to a depth of 8 km.

REFERENCES

Barka, A. A., Reilinger, R.,Saroglu, F., and Sengör, A.M.C. (1997), The Isparta Angle: its importance in the neotectonics of the Eastern Mediterranean Region, in *Proceedings of International Earth Science Colloquium on the Aegean Region*, edited, pp. 3-18, Izmir-Güllük, Turkey.

Chen, C. W., and H. A. Zebker (2000), Network approaches to two-dimensional phase unwrapping:intractability and two new algorithms, *Journal of the Optical Society of America A*, *17*(3), 401-414.

Costantini, M. (1998), A novel phase unwrapping method based on network programming, *Geoscience and Remote Sensing, IEEE Transactions on*, *36*(3), 813-821.

Curlander, J. C., and R. N. McDonough (1991), *Synthetic aperture radar : systems and signal processing*, Wiley, New York.

Eineder, M., Runge, H., Boerner, E., Bamler, R., Adam, N., Schattier, B., Breit, H., and Suchandt, S. (2004), SAR interferometry with TERRASAR-X, paper presented at European Space Agency, (Special Publication) ESA SP Proceedings of FRINGE 2003 Workshop.

Ekstrom, G., Dziewonski, A.M., Maternovskaya, N.N., and Nettles, M. (2005), Global seismicity of 2002: centroid-moment-tensor solutions for 1034 earthquakes, *Physics of the Earth and Planetary Interiors*, *148*(2), 303-326.

Emre, O., Duman, Tamer Yigit, Dogan, Ahmet, Ozalp, Selim, Tokay, Fatma, and Kuscu, Ismail (2003), Surface faulting associated with the Sultandagi earthquake (Mw 6.5) of 3 February 2002, southwestern Turkey, *Seismological Research Letters*, *74*(4), 382-392.

ESA (2007), http://envisat.esa.int/handbooks/asar/CNTR5-2.htm.

Fang, Z., Debao, M., and Huaining, P. (2004), A new baseline estimation approach based on the periodic interferometric phase, *Student Conference on Engineering Sciences and Technology, SCONEST 2004 Student Conference on Engineering Sciences and Technology, SCONEST 2004 - An International Multi-topic Conference by IEEE Student Branches at Jinnah University for Women, NED University of Engineering 2004*, 77-80.

Feigl, K. L., and E. Dupre (1999), RNGCHN: a program to calculate displacement components from dislocations in an elastic half-space with applications for modeling geodetic measurements of crustal deformation, *Computers & Geosciences*, *25*(6), 695-704.

Flynn, T. J. (1997), Two dimensional phase unwrapping with minimum weighted discontinuity, *Journal of the Optical Society of America A*, *14*(10), 2692-2701.

Gens, R. (2003), Two-dimensional phase unwrapping for radar interferometry: developments and new challenges, *International Journal of Remote Sensing*, *24*(4), 703 - 710.

Ghiglia, D. C., and M. D. Pritt (1998), *Two-dimensional phase unwrapping: theory, algorithms and software*, John Wiley and Sons Inc., New York.

Goyal, R. K., and A. K. Verma (1996), Mathematical formulation for estimation of baseline in synthetic aperture radar interferometry, *Sadhana-Academy Proceedings in Engineering Sciences*, *21*, 511-522.

Hanssen, R., and R. Bamler (1999), Evaluation of interpolation kernels for SAR interferometry, *IEEE Transactions on Geoscience & Remote Sensing*, *37*(1), 318-321.

Hanssen, R. F. (2001), *Radar interferometry : data interpretation and error analysis*, Kluwer Academic, Dordrecht ; Boston.

Jensen, J. R. (2000), *Remote sensing of the environment : an earth resource perspective*, 2nd ed. ed., Pearson Prentice Hall, Upper Saddle River, NJ

King, G. C., Stein, Ross S., and Rundle, John B. (1988), The growth of geological structures by repeated earthquakes; 1, Conceptual framework, *Journal of Geophysical Research*, *93*(B11), 13,307-313,318.

King, G. C. P., Stein, Ross S., and Lin, Jian (1994), Static stress changes and the triggering of earthquakes, *Bulletin of the Seismological Society of America*, *84*(3), 935-953.

Kocyigit, A., and A. A. Ozacar (2003), Extensional neotectonic regime through the NE edge of the outer Isparta Angle, SW Turkey; new field and seismic data, *Turkish Journal of Earth Sciences*, *12*(1), 67-90.

Lin, J., and R. S. Stein (2004), Stress triggering in thrust and subduction earthquakes and stress interaction between the southern San Andreas and nearby thrust and strike-slip faults, *Journal of Geophysical Research*, *109*(B2).

Maini, A. K., and V. Agrawal (2007), *Satellite technology : principles and applications*, John Wiley, Chichester, England ; Hoboken, NJ

McClusky, S., Balassanian, S., Barka, Aykut, Demir, C., Ergintav, S., Georgiev, I., Gurkan, O.,Hamburger, M., Hurst, K., Kahle, H., Kastens, K., Kekelidze, G., King, R., Kotzev, V., Lenk, O., Mahmoud, S., Mishin, A., Nadariya, M., Ouzounis, A., Paradissis, D., Peter, Y., Prilepin, M., Reilinger, R., Sanli, I., Seeger, H., Tealeb, A., Toksoz, M. N., and Veis, G. (2000), Global positioning system constraints on plate kinematics and dynamics in the eastern Mediterranean and Caucasus, *Journal of Geophysical Research*, *105*(B3), 5695-5719.

Ozer, N. (2006), New information on earthquake history of the Aksehir-Afyon Graben System, Turkey, since the second half of 18th century, *Natural Hazards and Earth System Sciences*, *6*(6), 1017-1023.

Reilinger, R., McClusky, Simon, Vernant, Philippe, Lawrence, Shawn, Ergintav, Semih, Cakmak, Rahsan, Ozener, Haluk, Kadirov, Fakhraddin, Guliev, Ibrahim, Stepanyan, Ruben, Nadariya, Merab, Hahubia, Galaktion, Mahmoud, Salah, Sakr, K., ArRajehi, Abdullah, Paradissis, Demitris, Al-Aydrus, A., Prilepin, Mikhail, Guseva, Tamara, Evren, Emre, Dmitrotsa, Andriy, Filikov, S. V., Gomez, Francisco, Al-Ghazzi, Riad, and Karam, Gebran (2006), GPS constraints on continental deformation in the Africa-Arabia-Eurasia continental collision zone and implications for the dynamics of plate interactions, *Journal of Geophysical Research*, *111*(B5).

Rosen, P. A., Hensley, S. , Joughin, I. R. , Li, F. K. , Madsen, S. N. , Rodriguez, E., and Goldstein, R. M. (2000), Synthetic aperture radar interferometry, *Proceedings of the IEEE, 88*(3), 333-382.

Skolnik, M. I. (1962), *Introduction to radar systems*, 2nd ed. ed., McGraw-Hill, New York.

Zebker, H. A., and R. M. Goldstein (1986), Topographic mapping from interferometric synthetic aperture radar observations, *Journal of Geophysical Research*, *91*(B5), 4993-4999.